International Journal of Greenhouse Gas Control xxx (2015) xxx–xxx

Contents lists available at ScienceDirect

International Journal of Greenhouse Gas Control

journal homepage: www.elsevier.com/locate/ijggc

Interaction between a fractured marl caprock and CO_2-rich sulfate solution under supercritical CO_2 conditions

Gabriela Dávila[a,b,c,*], Linda Luquot[a,b], Josep M. Soler[a,b], Jordi Cama[a,b]

[a] Institute of Environmental Assessment and Water Research (IDAEA), CSIC, Jordi Girona 18-26, 08034 Barcelona, Catalonia, Spain
[b] Associated Unit, Hydrogeology Group (UPC-CSIC), Spain
[c] Department of Geotechnical Engineering and Geosciences, Universitat Politècnica de Catalunya (UPC), Jordi Girona 1-3, 08034 Barcelona, Catalonia, Spain

ARTICLE INFO

Article history:
Received 25 June 2015
Received in revised form 31 October 2015
Accepted 4 November 2015
Available online xxx

Keywords:
CO_2 sequestration
Caprock
Fracture permeability
Calcite
Gypsum
Sealing

ABSTRACT

Geological CO_2 sequestration at pilot-plant scale will be developed at Hontomín (Spain). CO_2 will be injected into a limestone reservoir that contains a NaCl- and sulfate-rich groundwater in equilibrium with calcite and gypsum. The caprock site is composed of marl. The present study seeks to evaluate the interaction between the Hontomín marl and CO_2-rich sulfate solutions under supercritical CO_2 conditions (P_{Total} = 150 bar, pCO_2 = 61 bar and T = 60 °C).

Flow-through percolation experiments were performed using artificially fractured cores to elucidate (i) the role of the composition of the injected solutions (*S-free* and *S-rich* solutions) and (ii) the effect of the flow rate (0.2, 1 and 60 mL h^{-1}) on fracture permeability. Major dissolution of calcite (*S-free* and *S-rich* solutions) and precipitation of gypsum (*S-rich* solution) together with minor dissolution of the silicate minerals contributed to the formation of an altered skeleton-like zone (mainly made up of unreacted clays) along the fracture walls. Dissolution patterns changed from face dissolution to wormhole formation and uniform dissolution with increasing Peclet numbers.

In *S-free* experiments, fracture permeability did not significantly change regardless of the flow rate despite the fact that a large amount of calcite dissolved. In *S-rich* solution experiments, fracture permeability decreased under slow flow rates (0.2 and 1 mL h^{-1}) because of gypsum precipitation that sealed the fracture. At the highest flow rate (60 mL h^{-1}), fracture permeability increased because calcite dissolution predominated over gypsum precipitation.

1. Introduction

CO_2 geological storage in deep saline aquifers has been proposed as an alternative to emitting CO_2 to the atmosphere (Bachu, 2000; IPCC, 2005). Several industrial-scale geological CO_2 storage programs are already underway including the Norwegian Sleipner project in the North Sea (Korbøl and Kaddour, 1995) and the Weyburn project in Canada (Emberley et al., 2005). Characterization of field sites enables us to predict leakage risks and to design safe geological storage. Suitable formations should be deeper than 800 m (Benson and Cole, 2008). Under these conditions (P > 80 bar), sequestrated CO_2 will be stored as supercritical (SC) phase because of the in situ high pressure and temperature (P > 73.8 bar and T > 31.1 °C). CO_2 tends to float over brine (Birkholzer et al., 2009; Chabora and Benson, 2009) owing to the low density of $CO_{2\,(SC)}$, and subsequently comes into contact with the upper caprock. As a result of changes during CO_2 injection due to the increase in pressure and in brine acidification, as CO_2 dissolves and generates carbonic acid, minerals dissolve and precipitate. These changes can create or reactivate leakage pathways through abandoned and injection wells (Celia et al., 2005; Watson and Bachu, 2008; Angeli et al., 2009; Huerta et al., 2011; Abdoulghafour et al., 2013; Luquot et al., 2013), preexisting faults, fractures or microcracks in the caprock (Shukla et al., 2010), zones of high permeability (Deng et al., 2013) or through reactivation of faults (Angeli et al., 2009; Tongwa et al., 2013). The success of long-term CO_2 storage will ultimately depend on the caprock sealing capacity. Caprocks with low permeability (e.g., $k = 10^{-19}$ m^2 for Fjerritslev Formation of the Vedsted site in Denmark; Mbia et al., 2014) are suitable to prevent CO_2 leakages.

Research into the interaction between the caprock and CO_2-rich brine through potential leakage pathways is of paramount importance in order to evaluate caprock sealing capacity (Kaszuba et al., 2005; Noiriel et al., 2007; Andreani et al., 2008; Busch et al., 2008; Hangx et al., 2010; Ellis et al., 2011a,b; Berrezueta et al., 2013; Smith et al., 2013). Acidified CO_2-rich brines may react with caprock minerals that are susceptible to dissolution,

* Corresponding author at: Jordi Girona 18-26, Barcelona 08034, Catalonia, Spain.
E-mail address: gabgeo@cid.csic.es (G. Dávila).

http://dx.doi.org/10.1016/j.ijggc.2015.11.005
1750-5836/

releasing ions into the solution that could lead to mineral precipitation (Knauss et al., 1993; Brady and Carroll, 1994; Pokrovsky et al., 2009; Hellmann et al., 2010; Smith and Carroll, 2014). Mineralogical changes affect porosity, pore structure, and hydrodynamic and mechanical properties of caprocks (Park et al., 2011; Vilarrasa et al., 2013), potentially changing storage capacity (Alcalde et al., 2014).

In the last decade, caprock reactivity in CO_2-rich solutions has been studied by means of batch and flow-through experiments. Batch experiments were conducted from 80 to 300 bar of pCO_2 and from 50 to 250 °C for about 2 months to study the reactivity of different shales under supercritical CO_2 conditions (Kaszuba et al., 2005; Kohler et al., 2009; Alemu et al., 2011; Credoz et al., 2011; Liu et al., 2012; Garrido et al., 2013), showing significant mineral alterations and changes in pore volume owing to dissolution and precipitation of carbonate and clay minerals, illitization of smectite and formation of swelling clays.

In addition, flow-through laboratory-scale experiments under supercritical CO_2 conditions have been conducted to better understand how the caprock reactivity may affect the hydraulic and mechanical properties of the rocks. In these experiments, core and fractured core samples made up of marl, shale, limestone or evaporite rocks were used (Noiriel et al., 2007; Andreani et al., 2008; Angeli et al., 2009; Berrezueta et al., 2013; Ellis et al., 2011a,b; Deng et al., 2013; Smith et al., 2013). Other mineral alterations including reorganization of clay minerals in the fracture and an altered layer on the fracture surface led to variations in fracture permeability (Noiriel et al., 2007; Andreani et al., 2008).

Furthermore, a continuous exposure of the caprock allows formation of preferential dissolution paths, and brine circulates through these localized channels, creating a degraded zone. Likewise, re-activation of micro cracks plays an important role in the flow of CO_2 (Angeli et al., 2009). Ellis et al. (2011a,b) observed that the low content of clay minerals, compared with those in samples used by Noiriel et al. (2007), Andreani et al. (2008) and Angeli et al. (2009), prevents the formation of a continuous clay coating along the fracture. Moreover, local heterogeneity exerts strong control over the location of preferential pathways at the microscale (Smith et al., 2013). Ultimately, chemical reactions between the caprock and CO_2-rich solution lead to a change in fracture surface roughness and originate degraded zones with banding of reactive and non-reactive minerals (Deng et al., 2013).

CIUDEN (CIUdad De la ENergía) currently runs a demonstration pilot plant for CO_2 geological storage in a deep saline aquifer in Hontomín (northern Spain). In our work, CO_2 will be injected into a limestone reservoir rock at ca. 1500 m in depth ($P_{Total} \approx 150$ bar and $T \approx 60$ °C), which contains a sulfate-rich groundwater in equilibrium with calcite, dolomite and gypsum with an ionic strength of 0.6 M. The Hontomín caprock is mainly composed of marl (70 wt.% of calcite). The aim of the present work is to study the alteration of the Hontomín caprock in contact with CO_2-rich solutions under supercritical CO_2 conditions in order to assess the Hontomín caprock sealing capacity. Given the low permeability of the marl ($k < 10^{-18}$ m^2), the CO_2-rich water-caprock interaction may take place in preferential pathways (e.g., fractures or microcracks), which could lead to leakage and a decrease in sealing capacity. The present study focuses on the effects that solution composition and flow rate exert on the hydrodynamic and geochemical evolution of artificially fractured cores. Solution composition was varied by changing the concentration of sulfate and ionic strength (Na concentration) of the input solution. By reducing the sulfate concentration in equilibrium with respect to gypsum down to zero is possible to examine the role that gypsum precipitates have on fracture reactivity. The moderate change in Na concentration was set to account for a possible variability in the Na content in similar resident groundwaters and how this would affect the reactivity of the caprock. The flow rate vas varied from 0.2 to 60 mL h^{-1} to cover a broad range of fluid flow caused by increasing distances from the injection point and CO_2 overpressure during injection. To this end, and considering the experimental setups used in the studies mentioned above, flow-through percolation experiments were run at $P_{Total} = 150$ bar, $pCO_2 = 61$ bar and $T = 60$ °C, using three flow rates.

2. Materials and methods

2.1. Rock sample characterization

The marl used in this study was an outcrop sample from the Camino Formation provided by CIUDEN.

To characterize the mineralogical composition of the marl, X-ray diffraction (XRD) was performed on thoroughly crushed samples using a Bruker D8 A25 Advance X-ray diffractometer θ–θ, with CuKα1 radiation, Bragg-Brentano geometry, and a position sensitive LynxEyeXE detector. The diffractograms were obtained from 4° to 120° of 2-Theta with a step of 0.015° and a counting time of 0.5 s and the sample in rotation. The crystalline phase identification was carried out by using the computer program "EVA" (Produced by Bruker). The software TOPAS (Bruker AXS TOPAS, general profile and structure analysis software for powder diffraction data, V2.0, Bruker AXS, Karlsruhe, Germany, 2000) with the fundamental parameter approach was used for Rietveld refinement. The optimized parameters were background coefficients, zero-shift error, peak shape parameters, scale factor and cell parameters. The values of the pattern dependents, Rwp, disagreement factor, and statistical reliability factor of Bragg, RB, were evaluated and they indicated that fits are satisfactory. The Rwp obtained in all these measurements were less than 20, which indicates an accurate Rietveld refinement. Mineralogical composition of the washed sample was determined by Rietveld analyses with an uncertainty of 3 wt.% (Young, 1995). The XRD-Rietveld analyses were repeated in four samples to evaluate the sample heterogeneitiy and analytical uncertainty. The sample is composed of calcite (71.2 ± 2.9 wt.%), quartz (9.7 ± 0.4 wt.%), illite (7.1 ± 0.3 wt.%), albite (6.5 ± 0.3 wt.%), gypsum (2.0 ± 0.1 wt.%), clinochlore (2.8 ± 0.1 wt.%), anhydrite (0.5 ± 0.02 wt.%), and pyrite (0.2 ± 0.01 wt.%).

X-ray fluorescence (XRF) was performed to determine the chemical composition of the rock, calculate the compositional formula of the clinochlore and compare the iron concentration of the output solutions with the Fe content in the mineral. The sample was prepared mixing 0.3 g of crushed sample with 5.7 g of lithium tetraborate and 5 mg of lithium iodide as surfactant factor. The elemental composition was measured using an Axios Advanced spectrometer (PANalytical) equipped with Rh anode X-ray tube with a maximum power 2.4 kW. Mass balance was calculated to evaluate the clinochlore mineral formula from the XRD and XRF data, yielding $Mg_{2.9}Fe_{2.1}Si_3Al_2O_{10}(OH)_8$ (see Appendix A).

Seven cylindrical samples were cored from the rock provided. The samples were 9 mm in diameter and about 18 mm in length. The marl porosity (ϕ_i) was 7% as reported by CIUDEN ("ALM-09-008-2010"; Pujalte et al., 1998). Permeability was tested using the ICARE lab CSS II apparatus (Luquot et al., 2012) to evaluate the initial marl permeability. The permeability of the marl cores was lower than 10^{-18} m^2, which is the detection limit of the setup. As stated above, given this low permeability, the CO_2-rich water-caprock interaction may take place in preferential pathways (e.g., fractures or microcracks). Therefore, the experiments were performed using artificially fractured cores. A fracture was artificially created by sawing each core with a circular saw. The fracture in each core was laterally sealed using Duralco 4525 epoxy resin (stable mechanical and chemical properties up to 690 bar, 260 °C and low pH) to prevent any fracture closure throughout the

Please cite this article in press as: Dávila, G., et al., Interaction between a fractured marl caprock and CO_2-rich sulfate solution under supercritical CO_2 conditions. Int. J. Greenhouse Gas Control (2015), http://dx.doi.org/10.1016/j.ijggc.2015.11.005

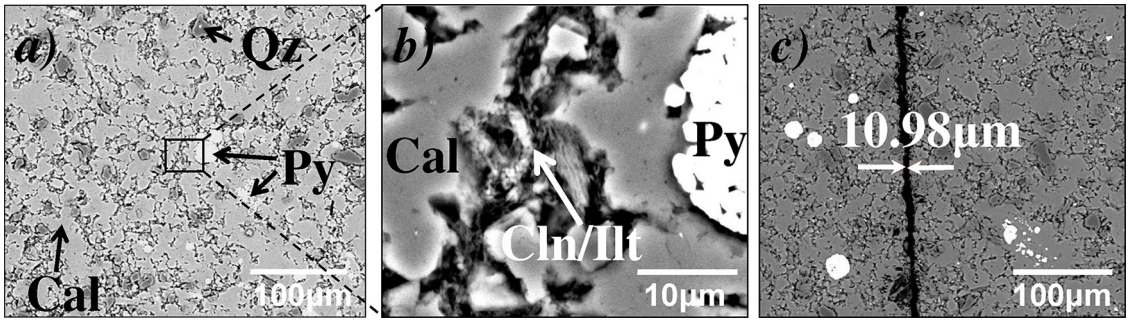

Fig. 1. ESEM backscattered electron images of a representative fractured core: (a) initial sample; (b) close up of the image in (a) and (c) view of the initial core fracture (aperture ~10 μm). Cal = calcite; Ilt = Illite; Py = pyrite; Clc = clinochlore and Qz = quartz.

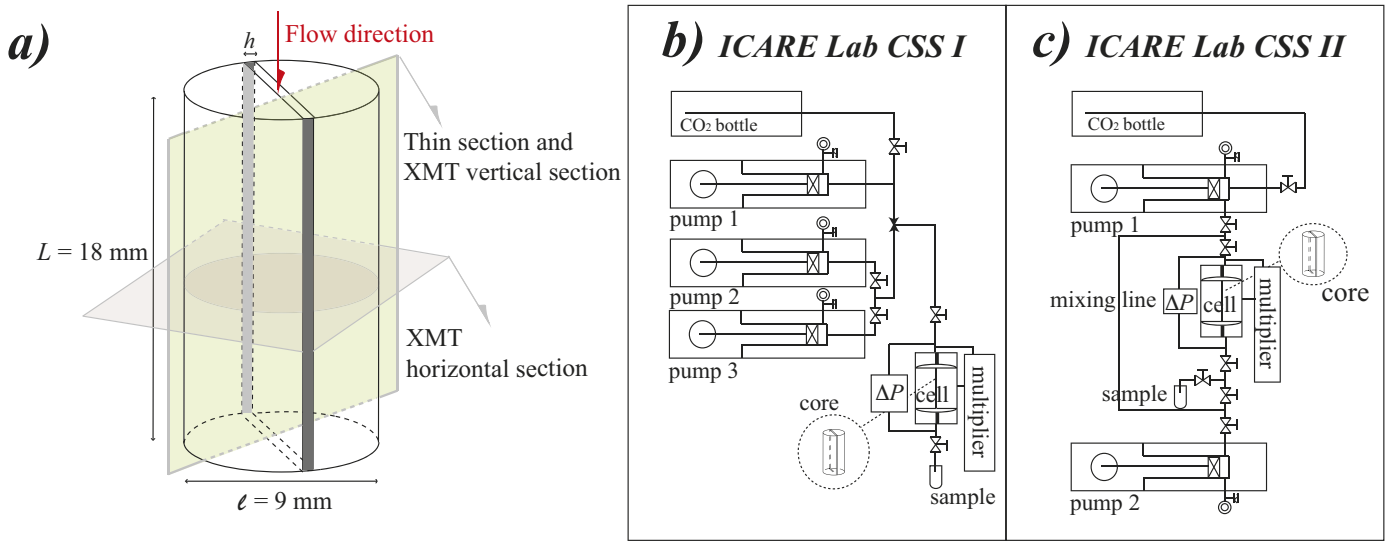

Fig. 2. Schemes showing: (a) the fractured core sample laterally sealed, (b) the ICARE Lab CSS I experimental setup and (c) the ICARE Lab CSS II experimental setup. CO_2 is added from a liquid CO_2 reservoir.

experiments and ensure solution circulation through the fracture. The core dimensions allowed examination of the unreacted and reacted cores by X-ray computed microtomography (XMT) with a good resolution (voxel size of 7.5 μm). XMT images were acquired at the ESRF (European Synchrotron Radiation Facility, Grenoble, France) using the ID19 beam line. The cores were mounted on a rotary stage and images were collected every 0.036° through a full 180° rotation using an exposure time of 0.25 s.

Thin sections parallel to the flow direction and perpendicular to the fracture were produced to characterize the fracture aperture before and after the experiments (Figs. 1c and 2a) and the dissolution/precipitation features by means of environmental scanning electron microscopy (ESEM). The thin sections were examined with a Hitachi H-4100FE instrument under a 15–20 kV potential in a high vacuum and using the backscattered electron detector (BSD). ESEM images of the thin sections before the experiment showed the morphologies of the grains, minerals composing the rock (Fig. 1a and b) and the aspect of the fractures (Fig. 1c). The initial fracture apertures ranged from 3 to 16 μm, yielding fracture volumes from 0.5 to 1.4 mm^3 (Table 1). Image segmentation processing was applied to both ESEM and XMT images to quantify the variation in mineral content using ImageJ software. This method allowed separation of rock and voids and measurement of the pore space between mineral grains over the whole image pack.

To identify possible secondary phases, MicroRaman spectroscopy analysis was performed on the thin sections of the reacted fractured cores, using a Jobin-Yvon LabRam HR 800 coupled with an Olympus BXFM optic microscope with a wavelength of 532 nm.

2.2. Injected solutions

Three synthetic solutions were prepared. Two sulfate-free solutions with respective ionic strength (I) of 0.3 and 0.6 M and a sulfate-rich solution with I = 0.6 M. The sulfate-free solutions were prepared to be equilibrated with respect to calcite at 25 °C by mixing analytical reagents (NaCl, $CaCl_2{\cdot}2H_2O$, $MgCl_2{\cdot}6H_2O$, KCl and NaBr; Table 2) and Millipore MQ water (18.2 MΩ cm). The sulfate-rich solution was meant to be an analog of the Hontomín reservoir groundwater, being equilibrated with respect to calcite, dolomite and gypsum at 25 °C by adding precise amounts of Na_2SO_4. The mixtures were stirred for 72 h and filtered using a 0.2 μm Nucleopore polycarbonate membrane filter. CO_2 was co-injected and mixed together with the *S-free* and *S-rich* solutions at P_{Total} = 150 bar and T = 60 °C. The dissolved $CO_{2(aq)}$ acidified the solution (Table 2), leading to undersaturation with respect to calcite. The concentration of CO_2 for both the *S-free* and *S-rich* solutions was 0.6 mol kgw^{-1}. The oxygen concentration was estimated to be 3.06×10^{-4} mol L^{-1} (atmospheric O_2 concentration (2.84×10^{-4} mol L^{-1}) plus the O_2 content impurities of the liquid CO_2 bottle). The saturation indexes of the injected solutions were calculated using the PhreeqC v.3 code (Parkhurst and Appelo, 2013) and the PhreeqC database. Initial solution pH was calculated by charge balance and was ≈3.2.

Please cite this article in press as: Dávila, G., et al., Interaction between a fractured marl caprock and CO_2-rich sulfate solution under supercritical CO_2 conditions. Int. J. Greenhouse Gas Control (2015), http://dx.doi.org/10.1016/j.ijggc.2015.11.005

Table 1
Experimental conditions of the experiments.

Exp.	Injected solutions	Q [mL h^{-1}]	t [h]	$h_{initial}$ [m]	τ [s]	$k_{f\text{-}initial}$ [m^2]
1	*S-free I* = 0.3	0.2	43	3.2×10^{-6}	10.0	8.8×10^{-13}
2	***S-rich I* = 0.6**	**0.2**	**35**	$\mathbf{3.8 \times 10^{-6}}$	**12.0**	$\mathbf{1.2 \times 10^{-12}}$
3	*S-free I* = 0.3	1	21	3.5×10^{-6}	2.0	1.0×10^{-12}
4	***S-rich I* = 0.6**	**1**	**70**	$\mathbf{1.6 \times 10^{-5}}$	**10.0**	$\mathbf{2.2 \times 10^{-11}}$
5	*S-free I* = 0.6	1	23	4.1×10^{-6} [a]	2.0	–
6	*S-free I* = 0.3	60	6	1.4×10^{-5}	0.1	1.7×10^{-11}
7	***S-rich I* = 0.6**	**60**	**7**	$\mathbf{1.6 \times 10^{-5}}$	**0.1**	$\mathbf{2.2 \times 10^{-11}}$

t: experimental duration.
$h_{initial}$ and $k_{f\text{-}initial}$: initial fracture aperture and fracture permeability, respectively.
τ: residence time.
[a] Permeability could not be measured. Aperture estimated from the ESEM image.

Table 2
Chemical composition and saturation indexes of the initial synthetic solutions.

Solutions	*S-free*		*S-free*		*S-rich*	
I [M]	0.3		0.6		0.6	
P [atm]	4×10^{-4}		4×10^{-4}		4×10^{-4}	
T [°C]	25		25		25	
			Concentration (mol kgw^{-1})			
Ca	2.1×10^{-2}		4.2×10^{-2}		5.1×10^{-2}	
Mg	1.6×10^{-2}		3.2×10^{-2}		3.2×10^{-2}	
K	5.7×10^{-3}		1.1×10^{-2}		1.1×10^{-2}	
Si	4.5×10^{-7}		4.5×10^{-7}		4.5×10^{-7}	
S	1.0×10^{-9}		1.0×10^{-9}		2.7×10^{-2}	
Na	2.0×10^{-1}		3.6×10^{-1}		3.9×10^{-1}	
Fe	7.2×10^{-9}		7.2×10^{-9}		7.2×10^{-9}	
Al	1.9×10^{-6}		1.9×10^{-6}		1.9×10^{-6}	
Cl	2.7×10^{-1}		4.8×10^{-1}		5.1×10^{-1}	
Br	5.7×10^{-3}		1.1×10^{-2}		1.1×10^{-2}	
			SI (PhreeqC)			
T [°C]	25	60	25	60	25	60
pH (charge balance)	7.64	3.25	7.57	3.20	7.55	3.26
pCO_2 [bar]	4×10^{-4}	61	4×10^{-4}	61	4×10^{-4}	61
			Mineral			
Calcite	0.00	−3.60	0.00	−3.49	0.00	−3.32
Dolomite	0.05	−6.97	0.07	−6.73	−0.02	−6.51
Anhydrite	−7.80	−7.61	−7.72	−7.54	−0.28	−0.08
Gypsum	−7.50	−7.66	−7.43	−7.59	0.01	−0.14
Quartz	−2.34	−2.80	−2.30	−2.77	−0.29	−0.76
Albite	−10.94	−20.23	−10.64	−20.26	−4.55	−14.24
Clinochlore	−10.71	−55.23	−9.93	−55.07	−4.29	−49.05
Illite	−14.08	−29.95	−13.70	−30.33	−6.68	−23.58
Pyrite	−122.15	−217.9	−116.57	−60.75	−101.58	−205.3
Kaolinite	−8.32	−17.85	−8.17	−18.36	−4.12	−14.62

K_{eq} values are from Phreeqc V.3 database except for gypsum which is from Garcia-Rios et al. (2014).

The total Ca, S, Mg, Si, Na, Al, K and Fe concentrations of the input and output solutions were analyzed by inductive coupled plasma-atomic emission spectrometry (ICP-AES) using a Perkin Elmer Optima 3200 RL. The detection limits for Ca, S, Mg, Si, Na, Al, K and Fe were 1.25×10^{-6}, 6.24×10^{-6}, 2.06×10^{-6}, 1.78×10^{-6}, 1.30×10^{-4}, 1.85×10^{-6}, 1.28×10^{-5} and 3.58×10^{-7} mol L^{-1}, respectively. The accuracy of the measurements was estimated to be 3%. Concentrations of chloride and bromide were not measured. The chemical compositions of the input and output synthetic solutions are listed in Table 2 and Tables S1 and S2 (supplementary data), respectively.

2.3. Experimental setup

Seven percolation experiments with different injected solutions and flow rates of 0.2, 1 and 60 mL h^{-1} were conducted using a flow-through system under reservoir conditions (P_{Total} = 150 bar and T = 60 °C; Fig. 2b and c). The percolation experiments carried out with flow rates of 0.2 and 1 mL h^{-1} were conducted with the ICARE Lab CSS II apparatus (see details in Luquot et al., 2012), which allows the solution to circulate under flow rates ranging from 0.05 to 40 mL h^{-1}. The ICARE Lab CSS I apparatus (see details in Luquot and Gouze, 2009), which permitted flow rates ranging between 0.6 and 180 mL h^{-1}, was used to conduct the experiments under the highest flow rate (60 mL h^{-1}). In the two apparatuses, and for all experiments, the sample confinement pressure was 180 bar. Experimental conditions and fracture properties are shown in Table 1.

During all experiments, the pressure drop between the inlet and the outlet of the fractured cores was continuously measured using a differential pressure sensor Rosemount 3051. Hence, using the measured pressure gradient (∇P) in Pa m^{-1} and combining the cubic law for flow (assuming that the fracture walls are represented by two smooth parallel plates; Huitt, 1956; Snow, 1969)

$$Q = -\frac{Wh^3}{12\mu}\nabla P \quad (1)$$

and Darcy's law

$$Q = -\frac{Ak_f}{\mu}\nabla P \quad (2)$$

Please cite this article in press as: Dávila, G., et al., Interaction between a fractured marl caprock and CO_2-rich sulfate solution under supercritical CO_2 conditions. Int. J. Greenhouse Gas Control (2015), http://dx.doi.org/10.1016/j.ijggc.2015.11.005

where W is the fracture width in m, h is the hydraulic aperture in m, μ is the viscosity of the fluid in Pa s, ∇P is the pressure gradient in Pa m^{-1}, A is the cross section area ($A = W{\cdot}h$) in m^2 and Q is the volumetric flow rate in m^3 s^{-1}, fracture permeability k_f (m^2) was calculated as

$$k_f = \frac{h^2}{12} \quad (3)$$

The volume of the fractures was estimated assuming a parallelepiped with h, L and W dimensions.

For each experiment, approximately 2 mL of the output solutions were continuously sampled. 0.5 mL were filtered using a syringe with a 0.2 μm Nuclepore™ polycarbonate membrane filter and 0.5 mL were not filtered. Both aliquots were immediately acidified in 9.5 mL of 1% HNO_3 solution (pH ≈ 1). This procedure avoided precipitation of Ca and Mg bearing carbonates during sample depressurization. Output solution concentrations of Ca, S, Mg, Si, Na, Al and K were measured by ICP-AES as were the input solutions. Variation in elemental concentrations between the filtered and non-filtered output solutions was ca. 3–5%, which practically coincided with the analytical uncertainty (3%). Therefore, it was decided to use the filtered output solutions which ensured lack of transported microparticles throughout the experiments.

3. Results and discussion

3.1. Dissolution and precipitation processes

3.1.1. Output concentrations

Fig. 3 shows variations in the aqueous chemistry with time in the sulfate-free (I = 0.3 and 0.6 M) and sulfate-rich (I = 0.6 M) experiments. ΔC_j accounts for the difference between the output and the input concentrations of element j ($\Delta C_j = C_{j(out)} - C_{j(in)}$). The error associated with ΔC_j ($\varepsilon(\Delta C_j)$) was estimated using the Gaussian error propagation method (Barrante, 1974) from the equation

$$\varepsilon(\Delta C_j) = \left[\varepsilon(C_{j(out)})^2 + \varepsilon(C_{j(in)})^2\right]^{\frac{1}{2}} \quad (4)$$

where $\varepsilon(C_{j(in)})$ and $\varepsilon(C_{j(out)})$ are the absolute errors associated with the input and output concentrations of element j, respectively, with an estimated uncertainty in the measured concentrations of 3% (ICP-AES). $\varepsilon(\Delta C_j)$ ranged from 10 to 40% for Ca and was around 3% for S, Fe and Si.

In *S-free* experiments at ionic strength of 0.3 and 0.6 M (Exps. 3 and 5; Table 1), similar variations in the Ca concentration, as well as very small changes in the S, Si and Fe output concentrations were observed over time (Fig. 3). Slight differences in concentrations can be attributed to different distributions of the primary iron- and silicon-bearing minerals (quartz, pyrite, illite, clinochlore and albite) along the fractures. The results suggest that in the I range of 0.3–0.6, the ionic strength effect on the mineral dissolution rates was negligible. This is in agreement with the small or negligible effect of ionic strength on gypsum and illite dissolution rates reported by Raines and Dewers (1997) and Bibi et al. (2011).

As for ΔCa (Fig. 3a), the excess of the Ca concentration was attributed to calcite dissolution. All input solutions were strongly undersaturated with respect to calcite (Table S3, supplementary data). The calculated input pH was 3.23 ± 0.03 (Table 2). Fig. 3b shows the ΔS variation with time. Dissolution of both gypsum and pyrite was expected in the *S-free* solution experiments (Table 2). However, since the pyrite dissolution rate (ca. 10^{-10} mol m^{-2} s^{-1} at pH from 3 to 5 and O_2 concentration of 3×10^{-4} mol L^{-1}; Domènech et al., 2002) was approximately six to seven orders of magnitude slower than that of gypsum (10^{-3} mol m^{-2} s^{-1}; Palandri and Kharaka, 2004), it was assumed that most of the released S was from dissolving gypsum. As the gypsum dissolution rate was not affected by dissolved CO_2 (Jeschke et al., 2001) or by pH, the ΔS decrease was probably caused by a decrease in the gypsum reactive surface area as gypsum dissolved (Fig. 3b). In the *S-rich* solution experiment the solution was in equilibrium with gypsum (Table 2). The early negative ΔS values (Fig. 3b), indicated precipitation of a *S-rich* mineral. MicroRaman spectra of the reacted solid samples (Exp. 4; see Appendix B) showed that the precipitated *S-rich* mineral was gypsum, ruling out anhydrite precipitation. This observation is in accordance with precipitation of gypsum in limestone column experiments that were run under the same P, T and pCO_2 conditions (Singurindy and Berkowitz, 2005; Garcia-Rios et al., 2014).

The ΔFe and ΔSi concentration tended to decrease with time in the two experiments (*S-free* and *S-rich* solutions; Fig. 3c,d). It was assumed that the Fe was mainly released from the clinochlore dissolution. Although the pyrite dissolution rate is much faster than that of clinochlore ($1–6 \times 10^{-12}$ mol m^{-2} s^{-1} at pH 3.2–5; Lowson et al., 2007), the content of pyrite was a factor of 14 smaller than that of clinochlore, resulting in a small pyrite reactive surface area that limited its dissolution. As for the Si concentration (Fig. 3d), since the injected solution was undersaturated with respect to illite, chlinochlore, albite and quartz, dissolution of the aluminosilicates and quartz could take place (Table 2). However, illite dissolution was unexpected or regarded as negligible because at pH 3 the illite rate constant (3×10^{-14} mol m^{-2} s^{-1}; Köhler et al., 2003) was two orders of magnitude lower than those of clinochlore (7×10^{-12} mol m^{-2} s^{-1}; Lowson et al., 2007) and albite (8×10^{-12} mol m^{-2} s^{-1}; Chou and Wollast, 1985). Given that the quartz dissolution rate constant (≈3×10^{-13} mol m^{-2} s^{-1} at pH 3.2; Bandstra et al., 2008) was also lower than those of chlinochlore and albite, Si was probably released from chlinochlore and albite. Moreover, the output solution was near equilibrium with respect to quartz (Table S3, supplementary data), which indicates that the quartz dissolution rate was even much slower. Accordingly, quartz, illite and pyrite dissolutions were omitted from the mass balance calculation shown in the following section.

ΔSi was about one order of magnitude lower than ΔFe in all experiments (Fig. 3c,d), yielding an aqueous Si/Fe ratio of around 0.1, which indicated a Si deficit based on the clinochlore stoichiometric ratio (Si/Fe = 1.4). Moreover, since albite dissolution would increase the aqueous Si/Fe ratio, it was assumed that some Si-bearing minerals could precipitate during the experiments. Actually, precipitation of kaolinite (Ketzer et al., 2009; Luquot et al., 2012; Yu et al., 2012) or precipitation of kaolinite and boehmite (Tutolo et al., 2015) were observed in other experiments where sandstone interacted with CO_2-rich brines. In the present study, the calculated *SI* values of the output solutions ranged from low undersaturation to low supersaturation with respect to kaolinite and boehmite (except Exp. 7) and showed high undersaturation with respect to smectite and muscovite (Table S3, supplementary data). In fact, this was not unexpected since the measured Al concentrations were always close to the ICP-AES detection limit (≈1.85×10^{-6} mol L^{-1}) probably because of precipitation of Al-bearing phases.

Although precipitation of kaolinite in the low-porosity rock matrix cannot be ruled out, inspection of the thin sections of the reacted samples by ESEM and microRaman spectroscopy showed no presence of kaolinite. Note that (see next section) the volume of precipitated kaolinite associated with the Si deficit along the fracture would be ~1 mm^3, making kaolinite detection difficult. At this point, it should be noted that, if kaolinite precipitation would not occur, the observed Si deficit could be associated with precipitation of less crystallized SiO_2 (amorphous silica gel). Otherwise, the solution remains undersaturated with respect to amorphous SiO_2 (Table S3, supplementary data).

Please cite this article in press as: Dávila, G., et al., Interaction between a fractured marl caprock and CO_2-rich sulfate solution under supercritical CO_2 conditions. Int. J. Greenhouse Gas Control (2015), http://dx.doi.org/10.1016/j.ijggc.2015.11.005

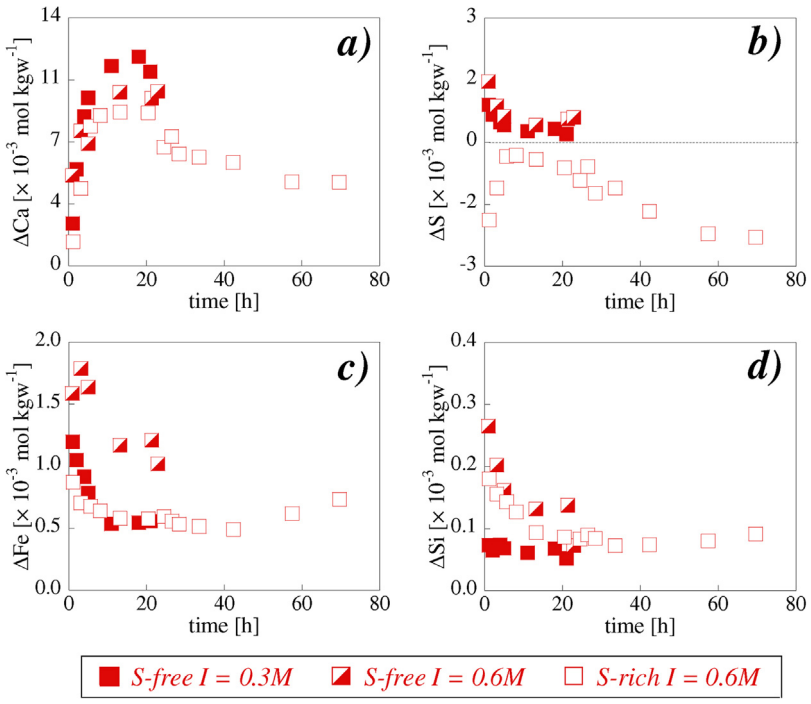

Fig. 3. Variation of the increment in the output *S-free* and *S-rich* solutions concentration vs. time in three experiments at 1 mL h^{-1} with *S-free* injected solutions (I = 0.3 and 0.6 M; Exps. 3 and 5, respectively) and with *S-rich* injected solution (I = 0.6 M; Exp. 4): (a) ΔCa, (b) ΔS, (c) ΔFe and (d) ΔSi.

Variations in the Na, K and Mg concentrations could not be determined because the small differences between the large input and output concentrations were within analytical error.

3.1.2. Influence of the flow rate

On the basis of dissolution of calcite, clinochlore and albite and precipitation of gypsum, and on the assumption that kaolinite precipitation took place, $C_{j(diss)}$ and $C_{j(ppt)}$ were calculated from the following mass balance equations

$$C_{j(out)} = C_{j(in)} + \sum_{1}^{N} C_{j(diss)} - \sum_{1}^{M} C_{j(ppt)} \quad (5)$$

where $C_{j(out)}$ is the total concentration of element j in the output solution, and N and M are the numbers of dissolved and precipitated minerals, respectively. For each element, Eq. (5) is given as

$$C_{S(out)} = C_{S(in)} + C_{S(Gp-diss)} - C_{S(Gp-ppt)} \quad (6)$$

$$C_{Ca(out)} = C_{Ca(in)} + C_{Ca(Cal-diss)} + C_{Ca(Gp-diss)} - C_{Ca(Gp-ppt)} \quad (7)$$

$$C_{Fe(out)} = C_{Fe(in)} + C_{Fe(Cln-diss)} \quad (8)$$

$$C_{Si(out)} = C_{Si(in)} + C_{Si(Cln-diss)} + C_{Si(Ab-diss)} - C_{Si(Kln-ppt)} \quad (9)$$

where gypsum, calcite, clinochlore, albite and kaolinite are termed *Gp*, *Cal*, *Clc*, *Ab* and *Kln*, respectively, and mineral dissolution or precipitation *-diss* or *-ppt*, respectively. In the *S-free* solution experiments, primary gypsum and anhydrite dissolved, yielding $C_{S(Gp-ppt)} = C_{Ca(Gp-ppt)} = 0$ in Eqs. (6) and (7), allowing calculation of S concentration from gypsum dissolution ($C_{S(Gp-diss)}$) and hence $C_{Ca(Gp-diss)}$. Contrary, in the *S-rich* solution experiments, gypsum and anhydrite precipitated, yielding $C_{S(Gp-diss)} = C_{Ca(Gp-diss)} = 0$ in Eqs. (6) and (7), allowing us to calculate $C_{S(Gp-ppt)}$ and hence $C_{Ca(Gp-ppt)}$. Regardless of the injected solution, Fe was released from clinochlore dissolution (Eq. (8)), allowing calculation of $C_{Fe(Cln-diss)}$ and stoichiometric $C_{Si(Cln-diss)}$. As mentioned, the measured Al concentrations were always close to the detection limit, preventing us from calculating the amount of dissolved albite and consequently the amount of precipitated kaolinite based on aluminum concentration. From Eq. (9) two mass balance calculations were therefore performed to estimate the concentration of dissolved albite and precipitated kaolinite. In the first calculation, albite dissolution was not assumed, thus Si was only released from clinochlore dissolution ($C_{Si(Ab-diss)} = 0$). In the second calculation, equal dissolution of albite and clinochlore was assumed ($C_{Si(Cln-diss)} = C_{Si(Ab-diss)}$), being Si released from both minerals.

As $C_{Ca(Cal-diss)}$ was computed, the calcite dissolution rate (R_{Cal} in mol s^{-1}) was calculated as

$$R_{Cal} = \frac{n_{Cal-diss}}{t} \quad (10)$$

where $n_{Cal-diss}$ is the total number of moles of dissolved calcite during the experiments

$$n_{Cal-diss} = \sum_{1}^{N} C_{Ca(Cal-diss)} Q \Delta t' \quad (11)$$

where $\Delta t'$ is the sampling time interval.

The effect of the flow rate on the chemical processes was firstly investigated from the variation in aqueous chemistry as a function of the number of equivalent water fracture volumes ($V_{ef} = t/\tau$) that circulated through the fracture and deduced from the R_{Cal} variation with the flow rate. V_{ef} was defined as the ratio between the experimental duration (t) and the residence time (τ, calculated as $\tau = V_{f\text{-}initial}/Q$; Table 1). Note that V_{ef} increased by increasing Q for the same experimental duration. Figs. 4 and 5 compare the variations in ΔCa, ΔS, ΔFe and ΔSi between experiments with *S-free* and *S-rich* injected solutions under different flow rates (0.2, 1 and 60 mL h^{-1}).

In the *S-free* experiments, Ca released from calcite dissolution was similar in the experiments run under slow flow rates (Q = 0.2 and 1 mL h^{-1}; Fig. 4a), but lower at 60 mL h^{-1} in which steady state was reached before the end of the experiment. Under slow flow rate conditions, R_{Cal} increased by speeding up the flow rate (4.4×10^{-10} mol s^{-1} at 0.2 mL h^{-1} and 1.6×10^{-9} mol s^{-1} at

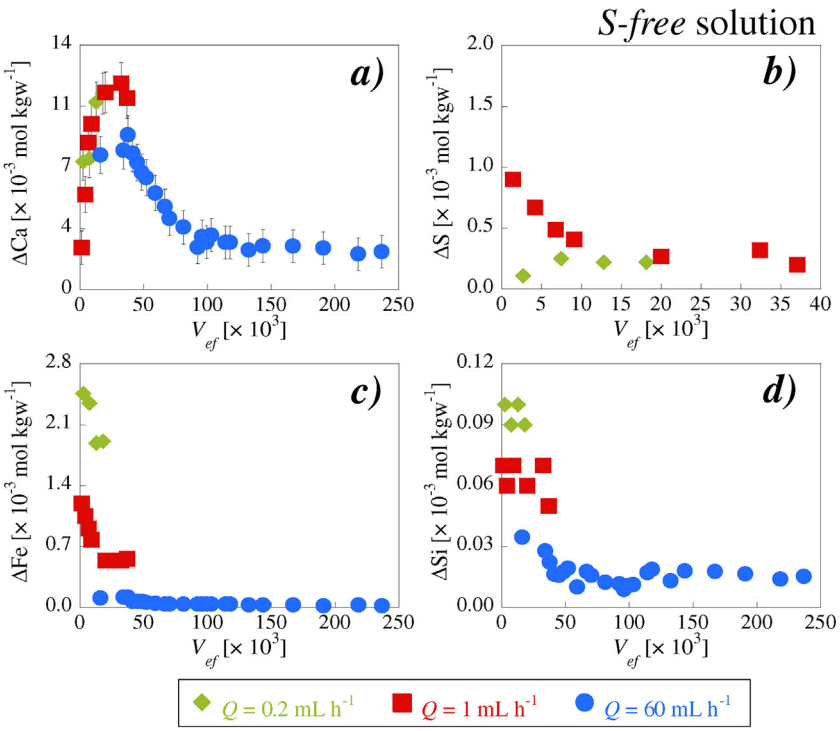

Fig. 4. Variation of solution composition with number of equivalent water fracture volumes (V_{ef}) under different flow rates [Q (mL h^{-1}) = 0.2 (Exp. 1), 1 (Exp. 3) and 60 (Exp. 6)] in *S-free* injected solution (I = 0.3 M): (a) ΔCa, (b) ΔS, (c) ΔFe and (d) ΔSi. pCO_2 = 61 bar, T = 60 °C.

1 mL h^{-1}, Table 3). At the highest flow rate (60 mL h^{-1}), the calcite dissolution rate (9.1 × 10^{-8} mol s^{-1}; Table 3) was one order of magnitude higher than that at 1 mL h^{-1}. ΔS was only measured in the experiments at 0.2 and 1 mL h^{-1} (Table 3), and the increase in the flow rate favored early gypsum dissolution (Fig. 4b).

In *S-rich* experiments, ΔCa was higher in the experiments run under slow flow rate conditions and nearly zero at the fastest flow rate (Fig. 5a). Reproducibility of the experimental results was verified by performing the 60 mL h^{-1} experiment twice. The short residence time of the solution prevented the Ca concentration

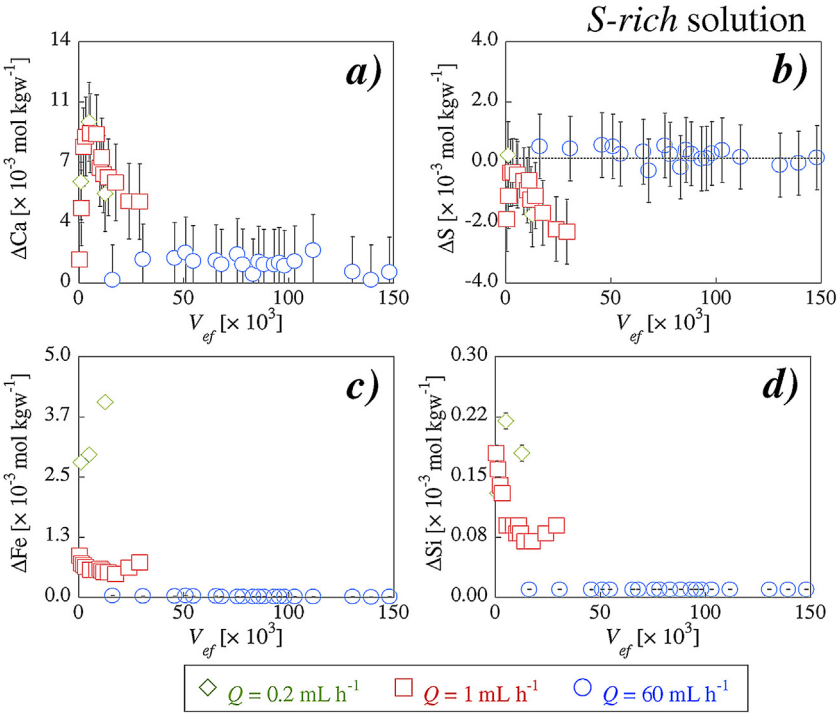

Fig. 5. Variation of solution composition with number of equivalent water fracture volumes (V_{ef}) under different flow rates [Q (mL h^{-1}) = 0.2 (Exp. 2), 1 (Exp. 4) and 60 (Exp. 7)] in *S-rich* injected solution (I = 0.6 M): (a) ΔCa, (b) ΔS, (c) ΔFe and (d) ΔSi. pCO_2 = 61 bar, T = 60 °C. Horizontal lines indicate zero increase in concentration.

Please cite this article in press as: Dávila, G., et al., Interaction between a fractured marl caprock and CO_2-rich sulfate solution under supercritical CO_2 conditions. Int. J. Greenhouse Gas Control (2015), http://dx.doi.org/10.1016/j.ijggc.2015.11.005

Table 3
Volume of initial fracture, volumes of dissolved calcite, gypsum, clinochlore and albite, volumes of precipitated kaolinite and gypsum, final volume of the fracture plus altered zone (pores) after reaction, Cal-diss/Gp-ppt volume ratio, and calcite dissolution rate in mol s^{-1}.

Exp.	Injected solution	Q [mL h^{-1}]	t [h]	$V_{Cal\text{-}diss}$ [mm^3]	$\varepsilon V_{Cal\text{-}diss}$ (%)	$V_{Gp\text{-}diss}$ or $V_{Gp\text{-}ppt}$ [mm^3]	$\varepsilon V_{Gp\text{-}diss}$ or $V_{Gp\text{-}ppt}$ (%)	$V_{Cln\text{-}diss}$ [mm^3]	$V_{Ab\text{-}diss}$ [mm^3]	$V_{Kln\text{-}ppt}$ [mm^3]	$\varepsilon V_{Cln\text{-}diss}$, $V_{Ab\text{-}diss}$ and $V_{Kln\text{-}ppt}$ (%)	$V_{f\text{-}initial}$ [mm^3]	$V_{diss\text{-}tot}$ [mm^3]	$V_{ppt\text{-}tot}$ [mm^3]	$V_{f\text{-}final}$ [mm^3]	$V_{Cal\text{-}diss}/V_{Gp\text{-}ppt}$	R_{Cal} [mol s^{-1}]
1	*S-free*	0.2	43	3.1	3	0.1	1	2.3	0–1.1	1.5–3.0[a]	1	0.6	5.4–6.4	1.6–3.2[a]	3.5–4.0	–	4.4×10^{-10}
2	***S-rich***	**0.2**	**35**	**2.8**	**10**	**0.4**[a]	**39**	**3.3**	**0–1.5**	**2.1–4.3**[a]	**2**	**0.7**	**6.1–7.6**	**1.5–2.7**[a]	**3.6–4.4**	**7.2**	$\mathbf{2.3 \times 10^{-10}}$
3	*S-free*	1	21	7.3	2	0.6	1	1.5	0–0.7	1.0–2.0[a]	1	0.6	8.8–9.5	1.6–2.6[a]	8.2–9.1	–	1.6×10^{-9}
4	***S-rich***	**1**	**70**	**20.3**	**2**	**7.2**[a]	**9**	**4.5**	**0–2.1**	**2.7–5.7**[a]	**1**	**2.8**	**24.9–26.9**	**9.9–12.9**[a]	**14.0–15.0**	**2.8**	$\mathbf{1.6 \times 10^{-9}}$
6	*S-free*	60	7	45.8	2	–	–	2.0	0–0.9	1.0–2.3	1	2.4	47.8–48.7	19.0–20.3[a]	48.8–46.8	–	9.1×10^{-8}
7	***S-rich***	**60**	**7**	**9.1**	**12**	**14.0**[a]	**32**	**1.2**	**0–0.5**	**0.6–1.4**[a]	**1**	**2.7**	**10.3–10.8**	**14.6–15.4**[a]	**12.1–13.4**	**0.7**	$\mathbf{8.3 \times 10^{-9}}$

t: experimental time; diss: dissolved mineral; ppt: precipitated mineral.
Cal: calcite, Gp: gypsum, Cln: clinochlore, Ab: albite, Kln: kaolinite.
$V_{f\text{-}initial}$: initial fracture volume, $V_{f\text{-}final}$: final fracture volume and R_{Cal}: calcite dissolution rate.
[a] Values indicate mineral precipitation.

from increasing. ΔS was negative in the experiments run under slow flow rates (Fig. 5b). Likewise, at 60 mL h^{-1}, the short residence time of the solution prevented the S concentration from decreasing (Fig. 5b). Like in *S-free* solution experiments, under slow flow rate conditions, calcite dissolution rate increased by speeding up the flow rate (from 2.3×10^{-10} mol s^{-1} at 0.2 mL h^{-1} to 1.6×10^{-9} mol s^{-1} at 1 mL h^{-1}, Table 3). At 60 mL h^{-1}, calcite dissolution rate (8.3×10^{-9} mol s^{-1}) was about one order of magnitude higher than that at 1 mL h^{-1}. Therefore, whatever the composition of the injected solution, an increase in the flow rate led to an increase in the calcite dissolution rate, which, being related to the degree of solution undersaturation with respect to calcite, suggests that the slower flow rate experiments resulted in a transport limiting reaction regime whereas the fast flow rate experiments were reaction rate limiting (Table S3, supplementary data). Nonetheless, slower calcite dissolution rates in the presence of sulfate could be favored by the formation of gypsum coatings on the surface of calcite grains, promoting calcite passivation (Offeddu et al., 2014).

As for the Fe and Si concentrations, in the two types of injected solution, an increase in flow rate resulted in a decrease in ΔFe and ΔSi (Figs. 4c,d and 5c,d) as residence time was shorter, lowering the dissolution rate of albite and clinochlore. Steady state was achieved in the experiment under the highest flow rate.

Also, the effect of the flow rate on the chemical processes was deduced from the variation in the volumes of dissolved and precipitated minerals. The volume of dissolved or precipitated mineral ($V_{min\text{-}diss}$ and $V_{min\text{-}ppt}$) was calculated as

$$V_{\min} = \nu_{\min} Q \int_{t'=0}^{t'=t} \alpha^{-1} C_j(t')\, dt' \tag{12}$$

where $\nu_{\min}$ is the molar volume of the mineral in m^3 mol^{-1}, α is the stoichiometric coefficient of element *j* in the mineral, C_j is the concentration of the element *j* from dissolved or precipitated mineral ($C_{j(diss)}$ or $C_{j(ppt)}$) in mol m^{-3} and *t* is the total experimental time. The molar volumes of calcite, clinochlore, gypsum, albite and kaolinite were calculated from the respective molecular weights and densities (Downs, 2006) to be 3.69×10^4, 2.26×10^5, 7.43×10^4, 1.00×10^5 and 9.82×10^4 mm^3 mol^{-1}, respectively.

In *S-free* solution experiments, the volume of dissolved calcite ($V_{Cal\text{-}diss}$) increased with flow rate (Table 3) as did the volume of dissolved gypsum ($V_{Gp\text{-}diss}$). Note that S concentration was not measured in the experiment at the highest flow rate (Fig. 4b). The volumes of dissolved clinochlore ($V_{Cln\text{-}diss}$) and albite ($V_{Ab\text{-}diss}$) and precipitated kaolinite ($V_{Kln\text{-}ppt}$) were almost the same under all flow rates. In *S-rich* solution experiments under slow flow rate conditions (0.2–1 mL h^{-1}), $V_{Cal\text{-}diss}$ and $V_{Gp\text{-}ppt}$ increased by speeding up the flow rate (Table 3), and the $V_{Cal\text{-}diss}/V_{Gp\text{-}ppt}$ ratio was always greater than one (Table 3), indicating dominancy of calcite dissolution over gypsum precipitation. At 60 mL h^{-1}, although $V_{Cal\text{-}diss}$ and $V_{Gp\text{-}ppt}$ were of the same order of magnitude as those at 1 mL h^{-1}, $V_{Gp\text{-}ppt} > V_{Cal\text{-}diss}$, yielding a slightly lower $V_{Cal\text{-}diss}/V_{Gp\text{-}ppt}$ ratio. $V_{Gp\text{-}ppt}$ tended to increase with the flow rate. $V_{Cln\text{-}diss}$, $V_{Ab\text{-}diss}$ and $V_{Kln\text{-}ppt}$ were almost the same at low flow rates but slightly lower at 60 mL h^{-1}.

Thus, based on the variation in the calculated volumes of dissolved and precipitated minerals and type of solution, it was observed that: (1) $V_{Cal\text{-}diss}$ tended to increase with flow rate regardless of the injected solution, except at 60 mL h^{-1} in the *S-rich* solution experiment; (2) $V_{Cln\text{-}diss}$ and $V_{Ab\text{-}diss}$ in *S-rich* solution were larger than those in *S-free* solution at 0.2 and 1 mL h^{-1} experiments, but not at 60 mL h^{-1} (Table 3); (3) as for $V_{Cln\text{-}diss}$ and $V_{Ab\text{-}diss}$, $V_{Kln\text{-}ppt}$ in *S-rich* solution was greater than that in *S-free* solution at 0.2 and 1 mL h^{-1}, showing an opposite trend at 60 mL h^{-1}. In all cases, regardless of the solution, the final pore volume associated with

Please cite this article in press as: Dávila, G., et al., Interaction between a fractured marl caprock and CO_2-rich sulfate solution under supercritical CO_2 conditions. Int. J. Greenhouse Gas Control (2015), http://dx.doi.org/10.1016/j.ijggc.2015.11.005

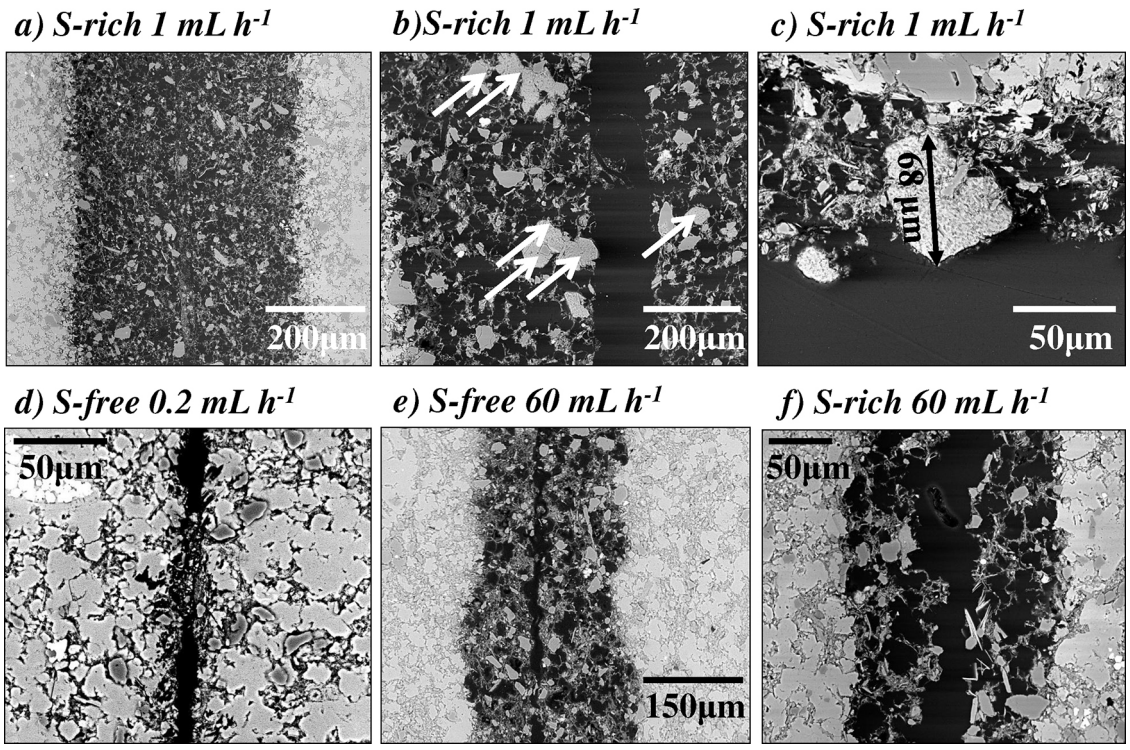

Fig. 6. ESEM images of several regions of the thin sections of the cores run in *S-free* and *S-rich* solution experiments under different flow rates. Top row: Exp. 4; (a) alteration at 8 mm from the inlet, (b) gypsum precipitation (indicated by arrows) and alteration at 12 mm from the inlet and (c) gypsum precipitate at 15 mm from the inlet. Bottom row: (d) fracture clogging (Exp. 1); (e) altered zone along the fracture wall (Exp. 6) and (f) altered zone along the fracture wall (Exp. 7).

the reacted core (volume of the final fracture plus volume of pores in the altered zone along the fracture wall), calculated as $V_{f\text{-}final} = V_{f\text{-}initial} + V_{Cal\text{-}diss} + V_{Gp\text{-}diss} + V_{Cln\text{-}diss} + V_{Ab\text{-}diss} - V_{Gp\text{-}ppt} - V_{Kln\text{-}ppt}$, was always larger than the initial fracture volume ($V_{f\text{-}initial}$), due to extensive calcite dissolution in all experiments, even if gypsum precipitated in the *S-rich* solution experiments (Table 3 and Fig. 6). Note that inclusion of the albite dissolution in the overall calculation barely affected the final volume associated with the reacted fracture because the albite dissolution was small owing to its low content (<6%).

3.2. Alteration of the rock

In the two *S-free* and *S-rich* solutions, a porous zone with a width (distance normal to fracture) up to ≈300 μm formed along the fracture walls during the experiments (Fig. 6). This was the result of significant calcite dissolution and, to a lesser extent, the dissolution of clinochlore and albite. The partially dissolved silicate grains and non-dissolved grains of quartz, pyrite and illite continued to be visible in the altered zone (Fig. 6a–d). The initial increase in ΔCa with time depicted in Figs. 4a and 5a indicated that calcite dissolution was favored by a high reactive surface area of the calcite grains. As the calcite dissolution progressed, the calcite reactive surface area close to the fracture diminished, leading to a ΔCa decrease until steady state was achieved. The diffusion through the remaining porous matrix of the altered zone limited further calcite dissolution (transport control of the reaction; see Exps. 6 and 4 in Figs. 4a and 5a).

In the experiments where the Ca concentration reached steady state (Exps. 6 and 4), a penetration length (x) corresponding to the zone next to the fracture affected by calcite dissolution was calculated using

$$x = \frac{V_{Cal-diss}}{2\ l\ L\ VF_{Cal}} \quad (13)$$

where $V_{Cal\text{-}diss}$ is the volume of dissolved calcite, l is the core diameter, L is the length of the core and VF_{Cal} is the volume fraction of calcite (0.66) in the fractured cores. Penetration lengths from ESEM and XMT images were measured and compared in the two experiments. In the *S-free* solution Exp. 6 (60 mL h^{-1}), x was 249 μm, which was approximately 11% smaller than the one measured (280 μm; Fig. 7a,b). In the *S-rich* solution Exp. 4 (1 mL h^{-1}), x was 176 μm, which was approximately 1% smaller than the one observed (180 μm; Fig. 7c).

Apparent diffusion coefficients (D_a, m^2 s^{-1}) at 60 °C were obtained in the experiments where the output Ca concentration reached steady state (Exp. 6: *S-free* solution and 60 mL h^{-1} and Exp. 4: *S-rich* and 1 mL h^{-1}; Figs. 4a and 5a). D_a values may indicate a possible effect of gypsum precipitation on the diffusion through the porous matrix of the altered zone. D_a values were calculated as $D_a = x^2/2t$, where x (m) is the penetration length (Eq. (13)), and t is time (s). By plotting x^2 as a function of time, D_a was calculated from the slope ($2D_a$) of the linear regression to be 2×10^{-12} (Exp. 6; $R^2 = 0.999$) and 1×10^{-13} m^2 s^{-1} (Exp. 4; $R^2 = 0.975$). One factor that probably contributed to the larger D_a in the *S-free* solution (Exp. 6) was a possible increase in tortuosity due to gypsum precipitation.

The increase in porosity over the reacted zone was estimated in two ways: (1) from representative regions of the fracture by ESEM images (ϕ_{ESEM}; Fig. 7a,c) and all fracture by XMT image (ϕ_{XMT}; Fig. 7b) and (2) from the calculated volumes of dissolved and precipitated minerals of the core expressed as $\phi_{VOL} = ((V_{Cal\text{-}diss} + V_{Gp\text{-}diss} + V_{Cln\text{-}diss} + V_{Ab\text{-}diss} - V_{Gp\text{-}ppt} - V_{Kln\text{-}ppt})/V_{total\text{-}cal}) + \phi_i$ where $V_{total\text{-}cal}$ is the volume of calcite if the core were composed of 100% calcite. In Exp. 6 (*S-free* solution), ϕ_{ESEM}, ϕ_{XMT} and ϕ_{VOL} were 65%, 48% and 67%, respectively. The difference between ϕ_{ESEM} and ϕ_{XMT} was attributed to the lower resolution of the XMT images (7.5 μm pixel^{-1}) compared with the ESEM (1 μm pixel^{-1}). Therefore, porosity in the reacted zone increased from 7% to ≈65%, which was similar to the volumetric fraction

Please cite this article in press as: Dávila, G., et al., Interaction between a fractured marl caprock and CO_2-rich sulfate solution under supercritical CO_2 conditions. Int. J. Greenhouse Gas Control (2015), http://dx.doi.org/10.1016/j.ijggc.2015.11.005

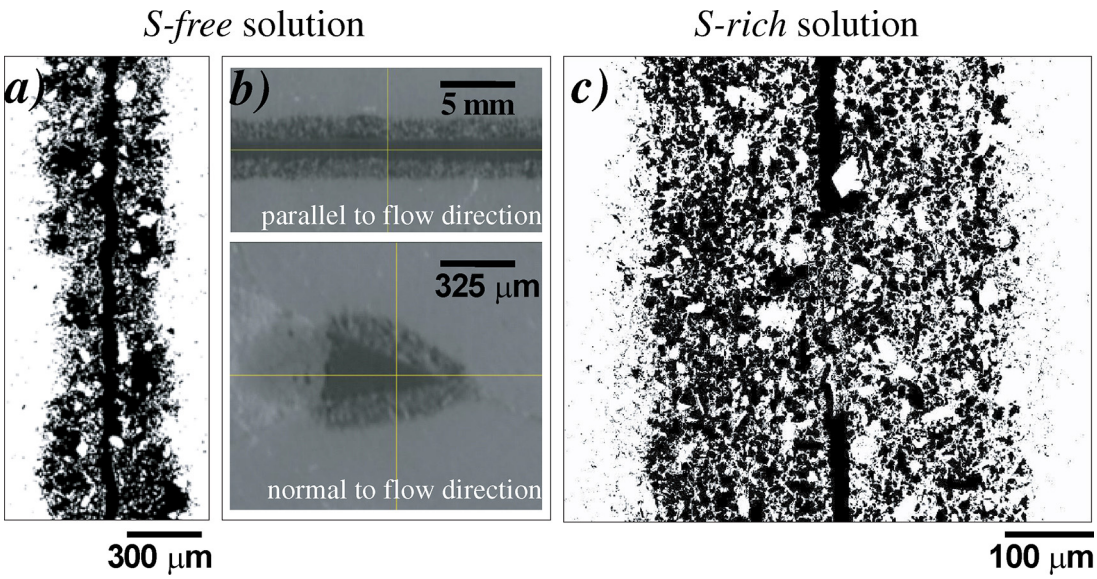

Fig. 7. Processed images: (a) ESEM image and (b) XMT image showing the altered zone along the fracture; the black background corresponds to pore space. (c) ESEM image showing the altered zone from where the pore space volume was calculated.

of calcite in the marl (≈66%), considering that calcite grains are uniformly distributed in the rock as well as along the core fracture. Hence, the dissolution of the calcite grains played a major role in the increase in porosity. In Exp. 4 (*S-rich* solution), the porosity was only calculated from the ESEM image and volume variation. $\phi_{ESEM} = \phi_{VOL} \approx 56\%$, which was much higher than the initial value, but lower than 65%. In this case, secondary gypsum contributed to a smaller increase.

3.3. Dissolution patterns

The adimensional Peclet number that correlates the diffusive and advective characteristic time scales ($Pe = h \cdot v/D_o$, h is the fracture aperture (m), v is the linear velocity (m s^{-1}), and D_o is the molecular diffusion coefficient of the solutes) was used to evaluate the role of solute transport in the mineral dissolution and precipitation processes along the fracture. The *Pe* values of the experiments were

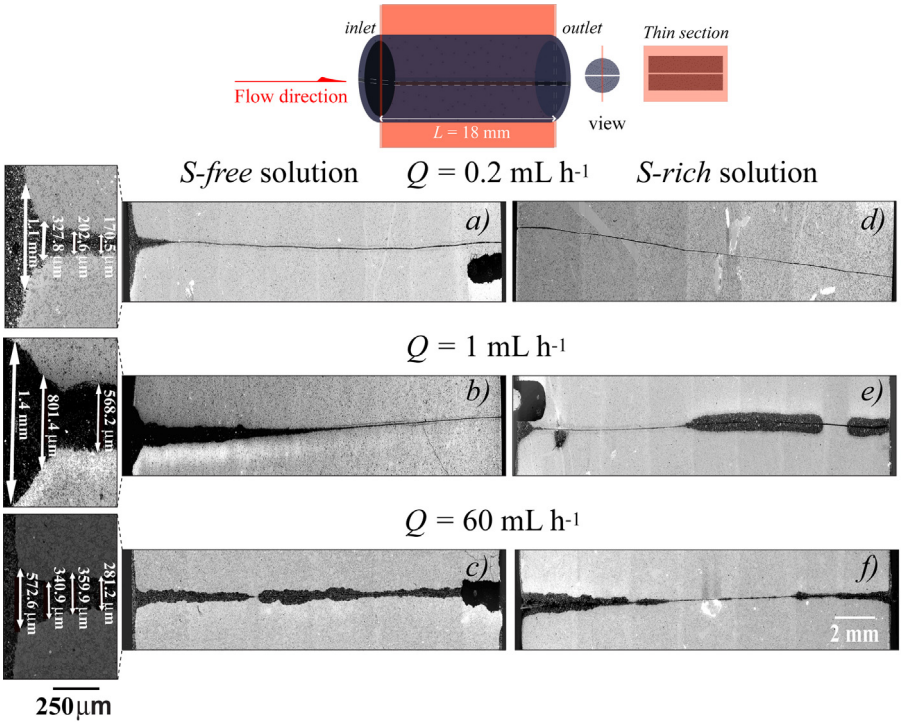

Fig. 8. ESEM images of thin sections parallel to flow direction of samples run under different flow rates: with *S-free* injected solution (a) $Q = 0.2$ mL h^{-1}, (b) $Q = 1$ mL h^{-1} and (c) $Q = 60$ mL h^{-1}, and with *S-rich* injected solution (d) $Q = 0.2$ mL h^{-1}, (e) $Q = 1$ mL h^{-1} and (f) $Q = 60$ mL h^{-1}. Note that the thin sections of (b), (c) and (f) were cut through the most altered zone, which is depicted by the arrows in Fig. 9.

Please cite this article in press as: Dávila, G., et al., Interaction between a fractured marl caprock and CO_2-rich sulfate solution under supercritical CO_2 conditions. Int. J. Greenhouse Gas Control (2015), http://dx.doi.org/10.1016/j.ijggc.2015.11.005

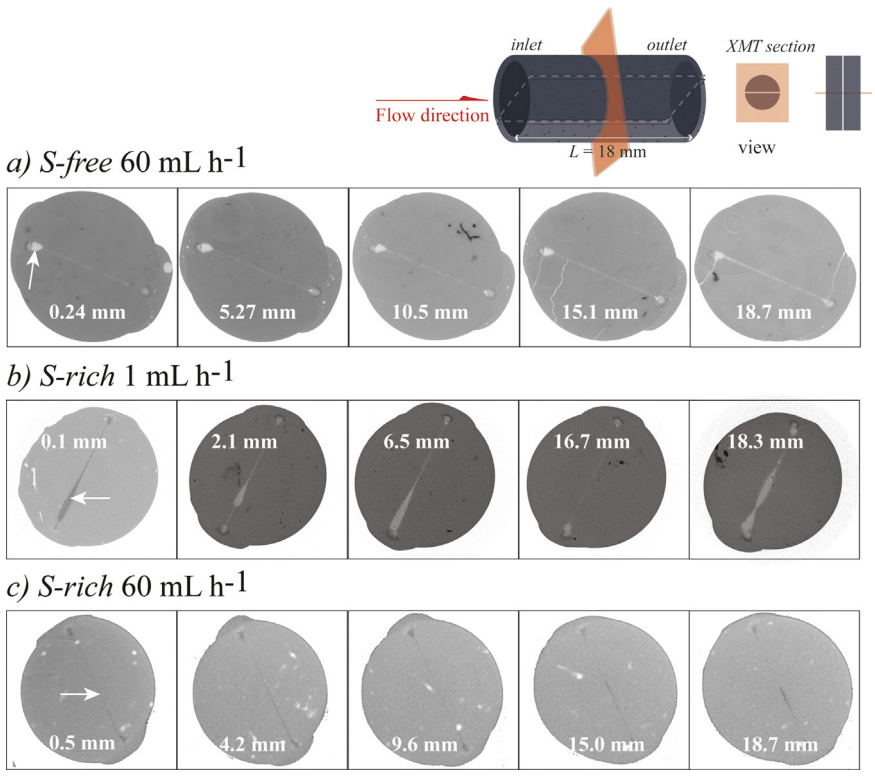

Fig. 9. XMT images normal to the flow direction showing the evolution of the dissolution pathways along the core length (a) *S-free* (Exp. 6), (b) *S-rich* (Exp. 4) and (c) *S-rich* (Exp. 7). The arrows indicate the altered zone where the thin sections were made (Fig. 8).

Table 4
Variation of the calculated fracture permeability and *Pe* number.

Exp.	Q [mL h^{-1}]	*Pe*	$h_{initial}$ [m]	$k_{f\text{-}initial}$ [m^2]	$k_{f\text{-}final}$ [m^2]	$k_{f\text{-}final}/k_{f\text{-}initial}$
1	0.2	4	3.2×10^{-6}	0.9×10^{-12}	0.7×10^{-12}	0.7
2	**0.2**	**4**	$\mathbf{3.8 \times 10^{-6}}$	$\mathbf{1.2 \times 10^{-12}}$	$\mathbf{0.04 \times 10^{-12}}$	**0.03**
3	1	21	3.5×10^{-6}	1.0×10^{-12}	0.8×10^{-12}	0.8
4	**1**	**21**	$\mathbf{1.6 \times 10^{-5}}$	$\mathbf{22.0 \times 10^{-12}}$	$\mathbf{0.2 \times 10^{-12}}$	**0.07**
6	60	1267	1.4×10^{-5}	17.0×10^{-12}	21.0×10^{-12}	1.2
7	**60**	**1267**	$\mathbf{1.6 \times 10^{-5}}$	$\mathbf{22.0 \times 10^{-12}}$	$\mathbf{84.0 \times 10^{-12}}$	**3.8**

$h_{initial}$: initial fracture aperture.

calculated assuming that D_o at 60 °C was 2×10^{-9} m^2 s^{-1} (Samson and Marchand, 2003), fracture apertures ranged from 3 to 10 μm and flow rates were 0.2, 1 and 60 mL h^{-1} (Table 4). The three *Pe* values obtained (4, 21 and 1267) were >1. Thus, solute transport in the fracture was controlled by advection in all experiments (e.g., Detwiler et al., 2000) regardless of the composition of the solutions.

Earlier studies show a certain correlation between distinct dissolution patterns in fractured cores and *Pe* numbers (Detwiler et al., 2003; Szymczak and Ladd, 2009; Elkhoury et al., 2013; Garcia-Rios et al., 2015). Elkhoury et al. (2013) reported that at low *Pe*, development of dissolution instabilities in fractured vuggy limestone cores led to face dissolution, intermediate *Pe* gave rise to large-scale channels, and a high *Pe* regime led to uniform dissolution along the fracture.

The respective ESEM and XMT images of the thin sections parallel and perpendicular to the flow direction (Fig. 8), taken at different positions along the fracture (Fig. 9), show the geometry of the dissolution patterns throughout the experiments. In *S-free* solution experiments, whereas fracture dissolution took place at 0.2 mL h^{-1} only near the inlet (Fig. 8a), larger dissolved region formed at 1 mL h^{-1} along the fracture (Fig. 8b). Therefore, face dissolution was observed at low *Pe* values (4 and 21). At the highest flow rate (60 mL h^{-1}) and the highest *Pe* (1267), dissolution occurred all along the fracture (Fig. 8c), resulting in a wormhole that probably originated in an existing local heterogeneity in the fracture (Figs. 8c and 9a). In *S-rich* solution experiments, at the lowest *Pe*, face dissolution initiated near the inlet (Fig. 8d). At *Pe* = 21, uniform dissolution developed in the first 16 mm of the fracture (Figs. 8e and 9b). From this point to the outlet, combination of wormhole and uniform dissolution occurred (Figs. 8e and 9b). For *Pe* = 1267, uniform dissolution predominated all along the fracture (Figs. 8f and 9c).

Therefore, as predicted by Elkhoury et al. (2013) and observed by Garcia-Rios et al. (2015), a *Pe* increase resulted in an evolution from face dissolution to wormhole and finally uniform dissolution. Nonetheless, it should be pointed out that local heterogeneities may control the overall dissolution pattern along the fractures, altering the predictions based on *Pe*.

3.4. Fracture permeability

Table 4 lists the calculated values of the initial fracture permeability ($k_{f\text{-}initial}$) of the fractures that ranged from 0.9×10^{-12} to 22×10^{-12} m^2 (Eq. (3)). Variations in fracture permeability with time are depicted in Fig. 10. In the *S-free* solution experiments, final k ($k_{f\text{-}final}$) was similar to the initial one in the three experiments,

Please cite this article in press as: Dávila, G., et al., Interaction between a fractured marl caprock and CO_2-rich sulfate solution under supercritical CO_2 conditions. Int. J. Greenhouse Gas Control (2015), http://dx.doi.org/10.1016/j.ijggc.2015.11.005

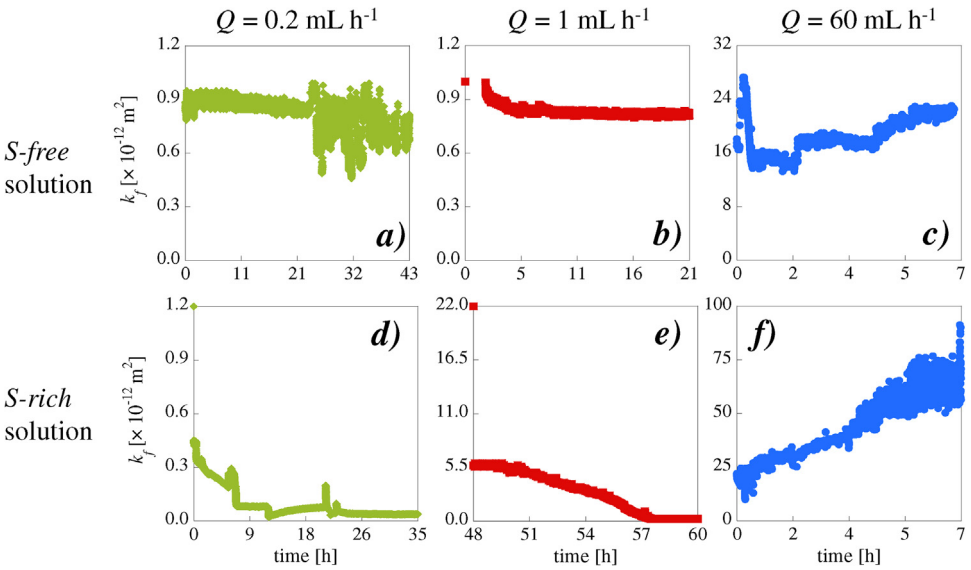

Fig. 10. Variation of fracture permeability, k_f, with time under different flow rates and solution compositions. In *S-free* solution experiments: (a) Exp. 1; (b) Exp. 3 and (c) Exp. 6. In *S-rich* solution experiments: (d) Exp. 2; (e) Exp. 4 and (f) Exp. 7.

yielding $k_{f\text{-}final}/k_{f\text{-}initial}$ ratios of 0.74, 0.81 and 1.24 at 0.2, 1 and 60 mL h^{-1}, respectively (Table 4 and Fig. 10a–c). A higher variation in k was expected given the considerable increase in pore volume ($V_{f\text{-}initial}$ and $V_{f\text{-}final}$; Table 3). This suggests that flow moved mainly through the initial fracture, with only diffusion in the reacted rock matrix. Under slow flow rates (Exps. 1 and 3), face dissolution resulted in about 85% of the fracture with negligible variations in the aperture (Fig. 8a,c), which could lead to slight changes in k_f. However, partial blocking of flow paths caused by (moving) grains is also a possibility, as shown in Figs. 6a,d,e and 7c. Noiriel et al. (2007) and Andreani et al. (2008) also reported minor changes in permeability in similar experiments with marls.

In *S-rich* solution experiments, $V_{f\text{-}final}$ increased by a factor that ranged from 4 to 5 (Table 3). In these experiments in contrast to the fairly constant k_f values obtained in the *S-free* experiments a dramatic k_f decrease was measured at the low flow rate range (Table 4 and Fig. 10d,e). This behavior was attributed to fracture sealing caused by gypsum precipitation ($V_{Gp\text{-}ppt}$ = 0.4 and 7.2 mm^3; Table 3 and Fig. 6a–c). Conversely, at the highest flow rate, k_f increased ($k_{f\text{-}final}/k_{f\text{-}initial} \approx 4$; Table 4 and Fig. 10f). In this experiment, gypsum precipitation was not observed.

Therefore, the experimental results showed that under slow flow rates, k_f remained constant in *S-free* experiments and decreased in *S-rich* experiments, whereas k_f increased in the two solutions under fast flow rate. This difference is greater in the *S-rich* solution experiments. The k_f variability depended on a number of factors: (i) effect of small differences (composition and/or structure) between different samples that influenced the reproducibility of the results (Chen et al., 2014), (ii) passivation of gypsum or inhibition of calcite dissolution in the presence of sulfate (Garcia-Rios et al., 2014; Offeddu et al., 2015) and (iii) movement of grains and blocking of flow paths, as illustrated in Fig. 6d.

4. Summary and conclusions

Flow-through percolation experiments under P_{Total} = 150 bar, pCO_2 = 61 bar and T = 60 °C (supercritical CO_2 conditions) with *S-free* and *S-rich* solutions injected at different flow rates (0.2, 1 and 60 mL h^{-1}) were run to better understand the reactivity of the Hontomín marl caprock.

Calcite dissolution was the main reaction because of the acidic character of the injected solutions under supercritical pCO_2. Results based on the experimental aqueous chemistry showed that the overall process was not affected by changing the ionic strength from 0.3 to 0.6 M. In *S-free* solutions, dissolution of calcite, primary gypsum, clinochlore and albite took place. In *S-rich* solutions in equilibrium with gypsum, dissolution of clinochlore and albite took place as did that of calcite, which promoted gypsum precipitation. A Si deficit suggests that dissolution of the silicate minerals trigger precipitation of Si-bearing secondary minerals (e.g., kaolinite or amorphous Si gel).

The dissolution and precipitation reactions controlled the variations in the final pore volume associated with the reacted core. In all experiments, an increase in the flow rate led to an increase in the calcite dissolution rate and in the final pore volume associated with the reacted core. In the *S-rich* solution, the volume of dissolved calcite was always larger than the volume of precipitated gypsum (except at 60 mL h^{-1}). The dissolution of calcite grains and, to a lesser extent, the dissolution of clinochlore and albite, created a high porosity zone (ϕ ranged from 48 to 67%) along the fracture walls. This porosity zone was composed of non-dissolved quartz, pyrite and illite grains, precipitated gypsum (in *S-rich* solutions) and Si-bearing phases (e.g., kaolinite or amorphous SiO_2).

As for the dissolution patterns, in the *S-free* solution experiments face dissolution occurred at slow flow rates (*Pe* of 4 and 21). At the highest flow rate (*Pe* = 1267), wormhole formation was observed. However, in *S-rich* solution experiments, face dissolution occurred only at the slowest flow rate. At an intermediate flow rate range, both uniform dissolution and wormhole took place. A combination of wormhole formation and uniform dissolution dominated at the highest flow rate. Local heterogeneities controlled mineral dissolution along the fracture, which could lead to unexpected dissolution patterns associated with *Pe* values.

As for the fracture permeability, at slow flow rate (low *Pe*), in *S-free* solution experiments, k_f did not significantly change since face dissolution did not cause fracture aperture to vary. Moreover, detached grains along the fracture may have led to the obstruction of the fluid flow, preventing k_f from increasing. In *S-rich* solutions, a marked decrease in k_f was attributed to gypsum precipitation. At fast flow rate (high *Pe*), k_f slightly increased with slight variations in aperture in the *S-free* solution. The increase in k_f in the *S-rich* experiment was attributed to the absence of gypsum precipitates. This suggests the existence of flow through the altered rock matrix.

Please cite this article in press as: Dávila, G., et al., Interaction between a fractured marl caprock and CO_2-rich sulfate solution under supercritical CO_2 conditions. Int. J. Greenhouse Gas Control (2015), http://dx.doi.org/10.1016/j.ijggc.2015.11.005

Nevertheless, small differences in composition and/or structure exist between different samples. These differences exert a considerable influence on the reproducibility of the experimental results, passivation of gypsum or inhibition of calcite dissolution in the presence of sulfate and movement of grains, and on the obstruction of flow paths. These phenomena play a central role in fracture permeability.

In the light of our findings, CO_2-rich solutions in contact with a fractured marl caprock favor CO_2 migration pathways if (1) groundwater has a low content of sulfate that prevents gypsum precipitation and/or if (2) the fluid flow is fast. By contrast, sealing of the fractures takes place if gypsum precipitates and the flow rates are slow.

Acknowledgements

Thanks are due to Javier Gargía-Veigas and Maite Romero from the Scientific and Technical Services of the University of Barcelona for technical assistance in the SEM-EDX and ICP-AES analyses and to Dr. Phillipe Gouze for the use of the flow-through percolation apparatus (ICARE Lab.) at the Laboratory of Geosciences of Montpellier (CNRS-University of Montpellier), France. We are indebted to Natàlia Moreno (IDAEA-CSIC) for her help in the XRD analyses and to Elisenda Seguí (CCiT-UB) for her assistance in the X-ray fluorescence analyses. GD is supported by a JAE-Predoc grant under the Program "Junta para la Ampliación de Estudios". LL is supported by a Juan de la Cierva postdoctoral grant (MINECO, Spain). This study was financed by the Compostilla OXYCFB300 project, Spanish Government Projects CGL2010-20984-C02-01 and CGL2014-54831-C3-1-R and the PANACEA project (European Community's Seventh Framework Programme FP7/2007–2013 under grant agreement number 282900). We also wish to thank the anonymous reviewers for their constructive comments that have improved the quality of the paper.

Appendix A.

The chemical composition of clinochlore ($Mg_XFe_YSi_3Al_2O_{10}(OH)_8$; $X+Y=5$) and the normative composition of the marl were calculated from the chemical (XRF, wt.% elements) and mineralogical (XRD-Rietveld analysis, wt.% minerals) compositions. Although Mg substitution for Ca in calcite can go up to 5–7% (Goldsmith et al., 1955) and albite can incorporate 10% K replacing Na (otherwise it is anorthoclase), in the calculation it is assumed that all Mg and K are from clinochlore and illite, respectively.

Ca (mol) in gypsum and anhydrite (Ca_{Gp+Anh}) was obtained from the total Ca (mol from XRF) and the Ca in calcite (mol from XRD-Rietveld).

$$Ca_{Gp+Anh} = Ca_{XRF} - Ca_{Cal-Rietveld} \quad (A1)$$

S (mol) in gypsum and anhydrite (S_{Gp+Anh}) was calculated using the stoichiometry

$$S_{Gp+Anh} = Ca_{Gp+Anh} \quad (A2)$$

S and Fe (mol) in pyrite (S_{Py} and Fe_{Py}) were calculated from

$$S_{Py} = S_{XRF} - S_{Gp} \quad (A3)$$

$$Fe_{Py} = \frac{S_{Py}}{2} \quad (A4)$$

and Fe and Mg (mol) in clinochlore (Fe_{Cln} and Mg_{Cln}) were obtained from

$$Fe_{Cln} = Fe_{XRF} - Fe_{Py} \quad (A5)$$

$$Mg_{Cln} = Mg_{XRF} \quad (A6)$$

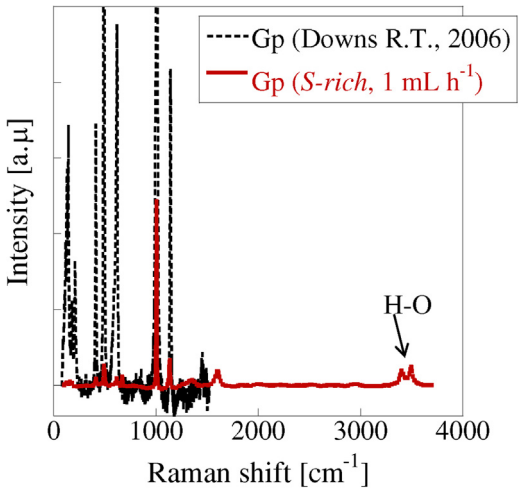

Fig. B1. The microRaman spectrum of a thin section prepared from Exp. 4 (*S-rich* solution, $Q = 1$ mL h^{-1}).

$$Mg_{Cln} + Fe_{Cln} = 5 \quad (A7)$$

$$\frac{Mg_{Cln}}{Fe_{Cln}} = Z \quad (A8)$$

resulting in: $Z = 1.38$; $X = 2.9$ and $Y = 2.1$ ($Mg_{2.9}Fe_{2.1}Si_3Al_2O_{10}(OH)_8$).

Al and Si (mol) in clinochlore (Al_{Cln} and Si_{Cln}) were calculated from the stoichiometry of the reaction:

$$Al_{Cln} = \frac{2}{5}(Mg_{Cln} + Fe_{Cln}) \quad (A9)$$

$$Si_{Cln} = \frac{3}{2}Al_{Cln} \quad (A10)$$

K (mol) in illite (K_{Ilt}) was calculated from the ideal stoichiometry of the mineral

$$K_{Ilt} = K_{XRF} \quad (A11)$$

$$Al_{Ilt} = 3K_{Ilt} \quad (A12)$$

$$Si_{Ilt} = 3K_{Ilt} \quad (A13)$$

Al (mol) in the albite (Al_{Ab}) was calculated from mass balance and the Na and Si (mol) in albite (Na_{Ab} and Si_{Ab}) were calculated using the stoichiometry of the reaction

$$Al_{Ab} = Al_{XRF} - Al_{Cln} - Al_{Ilt} \quad (A14)$$

$$Na_{Ab} = Al_{Ab} \quad (A15)$$

$$Si_{Ab} = 3Al_{Ab} \quad (A16)$$

Finally, the amount of Si in quartz (Si_{Qz}) corresponds to

$$Si_{Qz} = Si_{XRF} - Si_{Cln} - Si_{Ab} - Si_{Ilt} \quad (A17)$$

Appendix B.

Fig. B1

Appendix C. Supplementary data

Supplementary data associated with this article can be found, in the online version, at doi:10.1016/j.ijggc.2015.11.005.

References

Abdoulghafour, H., Luquot, L., Gouze, P., 2013. Characterization of the mechanisms controlling the permeability changes of fractured cements flowed through by CO_2-rich brine. Environ. Sci. Technol. 47, 10332–10338.

Alcalde, J., Marzán, I., Saura, E., Martí, D., Ayarza, P., Juhlin, C., Pérez-Estaún, A., Carbonell, R., 2014. 3D geological characterization of the Hontomín CO_2 storage site, Spain: multidisciplinary approach from seismic, well-log and regional data. Tectonophysics, 6–25.
Alemu, B.L., Aagaard, P., Munz, I.A., Skurtveit, E., 2011. Caprock interaction with CO_2: a laboratory study of reactivity of shale with supercritical CO_2 and brine. Appl. Geochem. 26, 1975–1989.
Andreani, M., Gouze, P., Luquot, L., Jouanna, P., 2008. Changes in seal capacity of fractured claystone caprocks induced by dissolved and gaseous CO_2 seepage. Geophys. Res. Lett. 35, L14404.
Angeli, M., Soldal, M., Skurtveit, E., Aker, E., 2009. Experimental percolation of supercritical CO_2 through a caprock. Energy Proc. 1, 3351–3358.
Bachu, S., 2000. Sequestration of CO_2 in geological media: criteria and approach for site selection in response to climate change. Energy Convers. Manage. 41, 953–970.
Bandstra, J.Z., Buss, H.L., Campen, R.K., Liermann, L.J., Moore, J., Hausrath, E.M., Navarre-Sitchler, A.K., Jang, J.-H., Brantley, S.L., 2008. Appendix: Compilation of mineral dissolution rates. In: Brantley, S.L., Kubicki, J.D., White, A.F. (Eds.), Kinetics of Water Rock Interactions. Springer, pp. 737–823.
Barrante, J.R., 1974. Applied Mathematics for Physical Chemistry. Prentice-Hall, New Jersey, pp. 256.
Benson, S.M., Cole, D.R., 2008. CO_2 sequestration in deep sedimentary formations. Elements 4, 325–331.
Berrezueta, E., González-Menéndez, L., Breitner, D., Luquot, L., 2013. Pore system changes during experimental CO_2 injection into detritic rocks: studies of potential storage rocks from some sedimentary basins of Spain. Int. J. Greenh. Gas Control 17, 411–422.
Bibi, I., Singh, B., Silvester, E., 2011. Dissolution of illite in saline–acidic solutions at 25 °C. Geochim. Cosmochim. Acta 75, 3237–3249.
Birkholzer, J., Zhou, Q., Tsang, C., 2009. Large-scale impact of CO_2 storage in deep saline aquifers: a sensitivity study on pressure response in stratified systems. Int. J. Greenh. Gas Control 3, 181–194.
Brady, P.V., Carroll, S.A., 1994. Direct effects of CO_2 and temperature on silicate weathering: possible implications for climate control. Geochim. Cosmochim. Acta 58, 1853–1856.
Busch, A., Alles, S., Gensterblum, Y., Prinz, D., Dewhurst, D.N., Raven, M.D., Stanjek, H., Krooss, B.M., 2008. Carbon dioxide storage potential of shales. Int. J. Greenh. Gas Control 2, 297–308.
Celia, M.A., Bachu, S., Nordbotten, J.M., Gasda, S.E., Dahle, H.K., 2005. Quantitative estimation of CO_2 leakage from geological storage: analytical models, numerical models, and data needs. In: Rubin, E.S., Keith, D.W., Gilboy, C.F. (Eds.), Greenhouse Gas Control Technologies, vol. I. Elsevier, pp. 663–671.
Chabora, E.R., Benson, S.M., 2009. Solution displacement and leakage detection using pressure measurements in aquifers overlying CO_2 storage reservoirs. Energy Proc. 1, 2405–2412.
Chen, L., Kang, Q., Viswanathan, H.S., Tao, W.Q., 2014. Pore-scale study of dissolution-induced changes in hydrologic properties of rocks with binary minerals. Water Resour. Res. 50, 9343–9365.
Chou, L., Wollast, R., 1985. Steady-state kinetics and dissolution mechanisms of albite. Am. J. Sci. 285, 963–993.
Credoz, A., Bildstein, O., Jullien, M., Raynal, J., Trotignon, L., Pokrovsky, O., 2011. Mixed-layer illite-smectite reactivity in acidified solutions: implications for clayey caprock stability in CO_2 geological storage. Appl. Clay Sci. 53, 402–408.
Deng, H., Ellis, B.R., Peters, C.A., Fitts, P., Crandall, D., Bromhal, G.S., 2013. Modifications of carbonate fracture hydrodynamic properties by CO_2-acidified solution flow. Energy Fuels 27, 4221–4231.
Detwiler, R.L., Glass, R.J., Bourcier, W.L., 2003. Experimental observations of fracture dissolution: the role of Peclet number on evolving aperture variability. Geophys. Res. Lett. 30, 1648.
Detwiler, R.L., Rajaram, H., Glass, R.J., 2000. Solute transport in variable-aperture fractures: an investigation of the relative importance of Taylor dispersion and macrodispersion. Water Resour. Res. 36, 1611–1625.
Domènech, C., Ayora, C., De Pablo, J., 2002. Oxidative dissolution of pyritic sludge from the Aznalcóllar mine (SW Spain). Chem. Geol. 190, 339–353.
Downs, R.T., 2006. The RRUFF Project: an integrated study of the chemistry, crystallography, Raman and infrared spectroscopy of minerals. In: Program and Abstracts of the 19th General Meeting of the International Mineralogical Association in Kobe, Japan (O03-13).
Elkhoury, J.E., Ameli, P., Detwiler, L.R., 2013. Dissolution and deformation in fractured carbonates caused by flow of CO_2-rich brine under reservoir conditions. Int. J. Greenh. Gas Control 16S, S203–S215.
Ellis, B., Peters, C., Fitts, J., Bromhal, G., Mcintyre, D., Warzinski, R., Rosenbaum, E., 2011a. Deterioration of a fractured carbonate caprock exposed to CO_2-acidified solution flow. Greenh. Gases Sci. Technol. 1, 248–260.
Ellis, B.R., Bromhal, G.S., McIntyre, D.L., Peters, C.A., 2011b. Changes in caprock integrity due to vertical migration of CO_2-enriched solution. Energy Proc. 4, 5327–5334.
Emberley, S., Hutcheon, I., Shevalier, M., Durocher, K., Mayer, B., Gunter, W.D., Perkins, E.H., 2005. Monitoring of fluid–rock interaction and CO_2 storage through produced fluid sampling at the Weyburn CO_2-injection enhanced oil recovery site, Saskatchewan, Canada. Appl. Geochem. 20, 1131–1157.
Garcia-Rios, M., Cama, J., Luquot, L., Soler, J.M., 2014. Interaction between CO_2-rich sulfate solutions and carbonate reservoir rocks from atmospheric to supercritical CO_2 conditions: experiments and modeling. Chem. Geol. 383, 107–122.
Garcia-Rios, M., Luquot, L., Soler, J.M., Cama, J., 2015. Influence of the flow rate on dissolution and precipitation features during percolation of CO_2-rich sulfate solutions through fractured limestone samples. Chem. Geol. 414, 95–108.
Garrido, D.R., Lafortune, S., Souli, H., Dubujet, P., 2013. Impact of supercritical CO_2/water interaction on the caprock nanoporous structure. Proc. Earth Planet. Sci. 7, 738–741.
Goldsmith, J.R., Graft, D.L., Joensuu, O.I., 1955. The occurrence of magnesian calcites in nature. Geochim. Cosmochim. Acta 7, 212–230.
Hangx, S.J.T., Spiers, C.J., Peach, C.J., 2010. The effect of deformation on permeability development in anhydrite and implications for caprock integrity during geological storage of CO_2. Geofluids 10, 369–387.
Hellmann, R., Daval, D., Tisserand, D., 2010. The dependence of albite feldspar dissolution kinetics on fluid saturation state at acid and basic pH: progress towards a universal relation. C. R. Geosci. 342, 676–684.
Huerta, N.J., Bryant, S.L., Strazisar, B.R., Hesse, M., 2011. Dynamic alteration along a fractured cement/cement interface: implications for long term leakage risk along a well with an annulus defect. Energy Proc. 4, 5398–5405.
Huitt, J.L., 1956. Fluid flow in simulated fractures. AlChE J., 259–264.
Intergovernmental Panel on Climate Change (IPCC), 2005. IPCC Special Report on Carbon Dioxide Capture and Storage. Cambridge University Press, Cambridge, UK, pp. 195–276 (Chapter 5).
Jeschke, A., Vosbeck, K., Dreybrodt, W., 2001. Surface controlled dissolution rates of gypsum in aqueous solutions exhibit nonlinear dissolution kinetics. Geochim. Cosmochim. Acta 65, 27–34.
Kaszuba, J.P., Janecky, D.R., Snow, M.G., 2005. Experimental evaluation of mixed fluid reactions between supercritical carbon dioxide and NaCl solution: relevance to the integrity of a geologic carbon repository. Chem. Geol. 217, 277–293.
Ketzer, J.M., Iglesias, R., Einloft, S., Dullius, J., Ligabue, R., de Lima, V., 2009. Water–rock–CO_2 interactions in saline aquifers aimed for carbon dioxide storage: experimental and numerical modeling studies of the Rio Bonito Formation (Permian), southern Brazil. Appl. Geochem. 24, 760–767.
Knauss, K.G., Nguyen, S.N., Weed, H.C., 1993. Diopside dissolution kinetics as a function of pH, CO_2, temperature, and time. Geochim. Cosmochim. Acta 57, 285–294.
Kohler, E., Parra, T., Vidal, O., 2009. Clayed cap-rock behavior in H_2O–CO_2 media at low pressure and temperature conditions: an experimental approach. Clay Clay Miner. 57, 616–637.
Köhler, S.J., Dufaud, F., Oelkers, E.H., 2003. An experimental study of illite dissolution kinetics as a function of ph from 1.4 to 12.4 and temperature from 5 to 50 °C. Geochim. Cosmochim. Acta 67, 3583–3594.
Korbøl, R., Kaddour, A., 1995. Sleipner vest CO_2 disposal-injection of removed CO_2 into the Utsira Formation. Energy Convers. Manage. 36, 509–512.
Liu, F., Lu, P., Griffith, C., Hedges, S.W., Soong, Y., Hellevang, H., Zhu, C., 2012. CO_2–solution–caprock interaction: reactivity experiments on Eau Claire shale and a review of relevant literature. Int. J. Greenh. Gas Control 7, 153–167.
Lowson, R.T., Brown, P.L., Comarmond, M.-C.J., Rajaratnam, G., 2007. The kinetics of chlorite dissolution. Geochim. Cosmochim. Acta 71, 1431–1447.
Luquot, L., Abdoulghafour, H., Gouze, P., 2013. Hydro-dynamically controlled alteration of fractured Portland cements flowed by CO_2-rich brine. Int. J. Greenh. Gas Control 16, 167–179.
Luquot, L., Andreani, M., Gouze, P., Camps, P., 2012. CO_2 percolation experiment through chlorite/zeolite-rich sandstone (Pretty Hill Formation – Otway Basin – Australia). Chem. Geol. 294–295, 75–88.
Luquot, L., Gouze, P., 2009. Experimental determination of porosity and permeability changes induced by injection of CO_2 into carbonate rocks. Chem. Geol. 265, 148–159.
Mbia, E.N., Frykman, P., Nielsen, C., Fabricius, I., Pickup, G.E., Bernstone, C., 2014. Caprock compressibility and permeability and the consequences for pressure development in CO_2 storage sites. Int. J. Greenh. Gas Control 22, 139–153.
Noiriel, C., Madé, B., Gouze, P., 2007. Impact of coating development on the hydraulic and transport properties in argillaceous limestone fracture. Water Resour. Res. 43, W09046.
Offeddu, F.G., Cama, J., Soler, J.M., Dávila, G., McDowell, A., Craciunescu, T., Tiseanu, I., 2015. Processes affecting the efficiency of limestone in passive treatments for AMD: column experiments. J. Environ. Chem. Eng. 3, 304–316.
Offeddu, F.G., Cama, J., Soler, J.M., Putnis, C.V., 2014. Direct nanoscale observations of the coupled dissolution of calcite and dolomite and the precipitation of gypsum. Beilstein J. Nanotechnol. 5, 1245–1253.
Palandri, J.L., Kharaka, Y.K., 2004. A compilation of rate parameters of water–mineral interaction kinetics for application to geochemical modeling. In: Science for a Changing World. U.S. Geol. Surv. Open File Report 2004-1068, p. 64.
Park, C.-H., Taron, J., Görke, U.-J., Singh, A.K., Kolditz, O., 2011. The fluidal interface is where the action is in CO_2 sequestration and storage: hydromechanical analysis of mechanical failure. Energy Proc. 4, 3691–3698.
Parkhurst, D.L., Appelo, C.A.J., 2013. Description of input and examples for PHREEQC version 3 – A computer program for speciation, batch-reaction, one-dimensional transport, and inverse geochemical calculations: U.S. Geological Survey Techniques and Methods, book 6., pp. 497 (Chapter A43).
Pokrovsky, O., Golubev, S.V., Schott, J., Castillo, A., 2009. Calcite, dolomite and magnesite dissolution kinetics in aqueous solutions at acid to circumneutral pH, 25 to 150 °C and 1 to 55 atm pCO_2: new constraints on CO_2 sequestration in sedimentary basins. Chem. Geol. 265, 20–32.
Pujalte, V., Robles, S., Hernández, J.M., 1998. La sedimentación continental del Grupo Campóo (Malm-Cretácico basal de Cantabria, Burgos y Palencia):

Please cite this article in press as: Dávila, G., et al., Interaction between a fractured marl caprock and CO_2-rich sulfate solution under supercritical CO_2 conditions. Int. J. Greenhouse Gas Control (2015), http://dx.doi.org/10.1016/j.ijggc.2015.11.005

testimonio de un reajuste hidrográfico al inicio de una fase rift. Cuadernos de Geología Ibérica 21, 227–251.
Raines, M., Dewers, T., 1997. "Mixed" kinetics control of fluid-rock interaction in reservoir production scenarios. J. Pet. Sci. Eng. 17, 139–155.
Samson, E., Marchand, J., 2003. Calculation of ionic diffusion coefficients on the basis of migration test results. Mater. Struct. 36, 156–165.
Shukla, R., Rajith, P., Haque, A., Choi, X., 2010. A review of studies on CO_2 sequestration and caprock integrity. Fuel 89, 2651–2664.
Singurindy, O., Berkowitz, B., 2005. The role of fractures on coupled dissolution and precipitation patterns in carbonate rocks. Adv. Water Resour. 28, 507–521.
Smith, M.M., Carroll, S.A.,2014. Experimental determination of chlorite kinetics at geothermal conditions. In: Thirty-Ninth Workshop on Geothermal Reservoir Engineering. Stanford University, Stanford, CA.
Smith, M.M., Sholokhova, Y., Hao, Y., Carroll, S.C., 2013. Evaporite caprock integrity: an experimental study of reactive mineralogy and pore-scale heterogeneity during brine-CO_2 exposure. Environ. Sci. Technol. 47, 262–268.
Snow, D.T., 1969. Anisotropic permeability on fractured media. Water Resour. Res. 6, 1273–1289.
Szymczak, P., Ladd, A.J.C., 2009. Wormhole formation in dissolving fractures. J. Geophys. Res. 114, B06203.
Tongwa, P., Nygaard, N., Blue, A., Bai, B., 2013. Evaluation of potential fracture-sealing materials for remediating CO_2 leakage pathways during CO_2 sequestration. Int. J. Greenh. Gas Control 18, 128–138.
Tutolo, B.M., Luhmann, A.J., Kong, X.Z., Saar, M.O., Seyfried, W.E., 2015. CO_2 sequestration in feldspar-rich sandstone: coupled evolution of fluid chemistry, mineral reaction rates, and hydrogeochemical properties. Geochim. Cosmochim. Acta 160, 132–154.
Vilarrasa, V., Carrera, J., Olivella, S., 2013. Hydromechanical characterization of CO_2 injection sites. Int. J. Greenh. Gas Control 1, 665–677.
Watson, T.L., Bachu, S., 2008. Identification of wells with high CO_2-leakage potential in mature oil fields developed for CO_2-enhanced oil recovery. In: SPE Paper 112924, SPE Improved Oil Recovery Symposium, 19–23 April, Tulsa, OK, USA.
Young, R.A., 1995. The Rietveld method. International Union of Crystallography Monographs on Crystallography, vol. 5. Oxford University Press, USA.
Yu, Z., Liu, L., Yang, S., Li, S., Yang, Y., 2012. An experimental study of CO_2-solution–rock interaction at in situ pressure–temperature reservoir conditions. Chem. Geol. 326–327, 88–101.

Please cite this article in press as: Dávila, G., et al., Interaction between a fractured marl caprock and CO_2-rich sulfate solution under supercritical CO_2 conditions. Int. J. Greenhouse Gas Control (2015), http://dx.doi.org/10.1016/j.ijggc.2015.11.005